12-18-2018

Additive Manufacturing of Ti6Al4V Alloy: A Review

Shunyu Liu

Yung C. Shin

Materials and Design 164 (2019) 107552

Contents lists available at ScienceDirect

Materials and Design

journal homepage: www.elsevier.com/locate/matdes

Additive manufacturing of Ti6Al4V alloy: A review

Shunyu Liu, Yung C. Shin *

Center for Laser-based Manufacturing, School of Mechanical Engineering, Purdue University, West Lafayette, IN 47906, USA

HIGHLIGHTS

- Recent progresses in additively manufactured Ti6Al4V were reviewed.
- Laser direct deposition, selective laser melting and electron beam melting were comparatively studied.
- Processing-microstructure-tensile and fatigue properties relationship were established.
- Effects of defects on mechanical properties were also addressed.

GRAPHICAL ABSTRACT

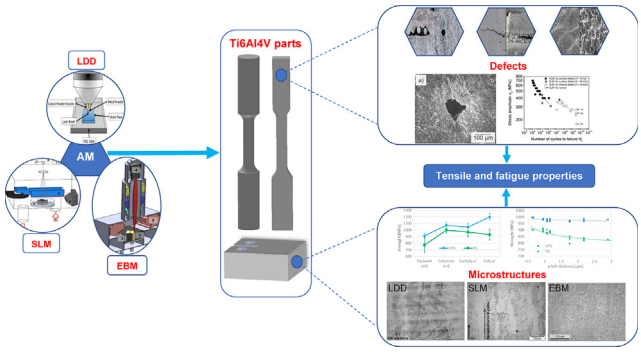

ARTICLE INFO

Article history:
Received 14 November 2018
Received in revised form 10 December 2018
Accepted 13 December 2018
Available online 18 December 2018

Keywords:
Ti6Al4V
Directed energy deposition
Selective laser melting
Electron beam melting
Tensile property
Fatigue property

ABSTRACT

In this paper, the recent progress on Ti6Al4V fabricated by three mostly developed additive manufacturing (AM) techniques-directed energy deposition (DED), selective laser melting (SLM) and electron beam melting (EBM)-is thoroughly investigated and compared. Fundamental knowledge is provided for the creation of links between processing parameters, resultant microstructures and associated mechanical properties. Room temperature tensile and fatigue properties are also reviewed and compared to traditionally manufactured Ti6Al4V parts. The presence of defects in as-built AM Ti6Al4V components and the influences of these defects on mechanical performances are also critically discussed.

1. Introduction

Ti6Al4V alloy, also known as Ti64, is an $\alpha + \beta$ titanium alloy with high strength, low density, high fracture toughness, excellent corrosion resistance and superior biocompatibility [1,2]. Recognized as the most popular titanium alloy, Ti6Al4V occupies almost a half of the market share of titanium products used in the world today. Ti6Al4V alloy was originally developed for aircraft structural applications in 1950s. This lightweight and yet strong alloy saves weight in highly loaded structures and is hence extremely suitable for jet engines, gas turbines and many airframe components [3–6]. While the aerospace industry still dominates the Ti6Al4V demand [4–7], other application fields such as marine, automobile, energy, chemical and biomedical industries have also found its wide acceptance during the last half a century. The low density, high strength, high corrosion resistance and biocompatibility are attractive characteristics of Ti6Al4V for applications such as bridges and implants [2,8–12]. Its applications have also been extended to the marine and chemical industries due to its high corrosion resistance to most corrosive acids and alkalis [2,13–15].

Despite the high demand, manufacture of Ti6Al4V products is always challenging due to its poor thermal conductivity [16], the

* Corresponding author.
E-mail address: shin@purdue.edu (Y.C. Shin).

https://doi.org/10.1016/j.matdes.2018.107552

propensity to strain hardening [17,18] and active chemical reactivity to oxygen [19]. Conventional manufacture of Ti6Al4V products relies on forging, casting and rolling of bulk feedstock materials, followed by subsequent machining to final shapes and dimensions. These traditional manufacturing processes always inevitably result in a large amount of material waste, high manufacturing cost and long lead time [20,21]. Under such circumstances, additive manufacturing (AM), an advanced manufacturing technology of producing near-net shape structures directly from CAD models by adding materials in a layer-by-layer fashion, offers its beneficial capability for fabrication of Ti6Al4V products with geometric complexities [6,20]. Fig. 1 illustrates some of Ti6Al4V structures built by DED, SLM and EBM processes.

Compared to traditional manufacturing methods, the most significant advantage of AM is its freeform fabrication capability of complex parts directly from feedstock materials without involving traditional manufacturing methods such as extrusion, forging, casting and secondary machining processes to achieve desired shapes [22–27]. The near-net shaping capability makes AM a cost-effective technique due to its waste minimization. For example, the "buy-to-fly" ratio (the mass ratio between the raw material used to produce a component and the mass of the component) is 12–25:1 for aircraft titanium products made by traditional manufacturing methods [20], while it drops to 3–12:1 for a typical titanium component manufactured by AM processes [25,28]. Furthermore, AM has high flexibility on feedstock material types [29], and unconsumed powders can be reused, making it more cost-efficient [30,31].

AM processes include a large range of versatile methods. With respect to the fabrication of dense metallic structures, powder-based AM techniques such as DED, SLM and EBM are mostly used [22,23,26]. In these processes, a laser or electron beam interacts with feedstock powders and produces a molten pool, where rapid melting and resolidification takes place [38]. Due to the highly localized heat input and short interaction time, large temperature gradients and high cooling rates are present [39,40]. These unique thermal features dramatically affect as-built microstructures and lead to high residual stresses in AM built Ti6Al4V products, which in turn govern their macroscopic performances [16,41]. Moreover, the inevitably formed defects during the AM processes will significantly deteriorate the products' mechanical and fatigue properties [42–44].

Regarding service quality and durability, the material properties of final products, particularly mechanical properties, are the most important ones to decide whether AM processes can be acceptable manufacturing techniques in lieu of traditional methods. Therefore, the quality assessment of AM Ti6Al4V products should consider

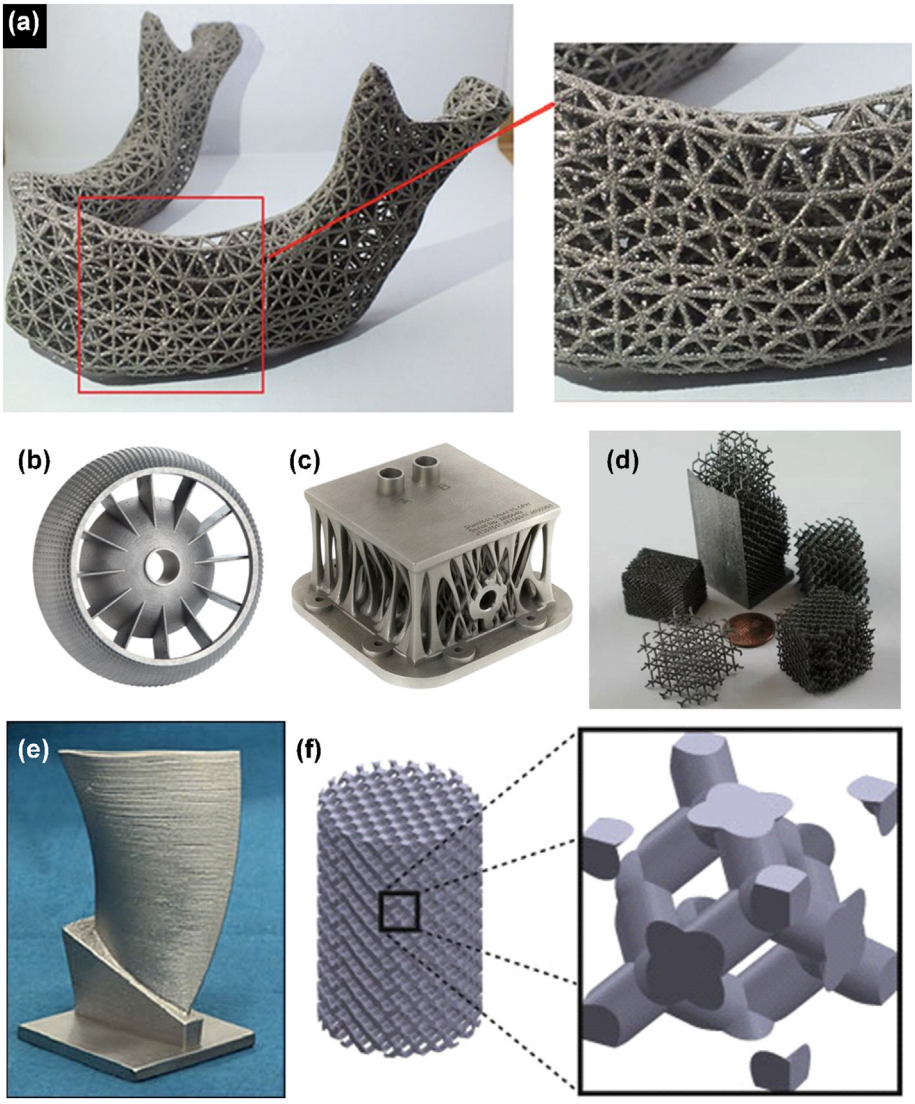

Fig. 1. (a) 3D mesh Ti6Al4V mandibular prosthesis scaffold fabricated using EBM [32]. (b) Air duct made of Ti6Al4V produced by SLM in high precision without major rework [33]. (c) Ti6Al4V medical parts built by EBM [34]. (d) Lattice-structured Ti6Al4V foams built using EBM [35]. (e) Ti6Al4V blade built using DED [36]. (f) Ti6Al4V porous sample and the diamond unit cell built using SLM. Reproduced with permission from Elsevier [37].

practical application requirements and the performance should be compared with the counterparts built with traditional manufacturing methods. For Ti6Al4V, the foremost demand is for its load-bearing applications, and thus tensile and fatigue performances are the key properties to consider. Although many papers have discussed these properties (results are summarized in Tables 3 and 4), a very limited amount of work covered a compressive study to make a comparison between DED, SLM and EBM fabricated Ti6Al4V structures on the vital combination of manufacture, microstructures and resulting properties as well as the effects of defects.

This paper summarizes the latest findings on AM Ti6Al4V and compares the tensile and fatigue properties to those of traditionally manufactured Ti6Al4V. Some experimental and simulation studies conducted by the authors are also compared with the recent progress revealed in literature. The goal of this paper is aimed at establishing the processing-microstructure-property relationship for the additively manufactured Ti6Al4V using DED, SLM and EBM techniques. The presence of defects and the effects of these defects on the performance of final products are also thoroughly addressed. Although hot isostatic pressing (HIP) [45–48] and heat treatment [47,49–51] have been proved to be effective in alleviating some of the fabrication limitations, the as-built parts with complex geometries, i.e., the lattice-structured products exhibited in Fig. 1 would lose shape accuracy if subjected to HIP, while heat treatment may not produce a consistent microstructure for irregular-shaped samples. In addition, these post-processing treatments increase the overall cost. Therefore, this paper only focuses on AM Ti6Al4V in the as-built condition. The knowledge included in this paper can serve as a guidance to tailor the limitations of AM processes in the manufacture of Ti6Al4V products, and thus promotes the wide feasibility of AM Ti6Al4V in critical load-bearing applications.

2. Additive manufacturing

2.1. Working principle

The ASTM F42 Technical Committee defines AM as the "process of joining materials to make objects from three-dimensional (3D) model data, usually layer upon layer, as opposed to subtractive manufacturing methodologies" [52]. It includes various near-net shaping processes that are capable of building complex 3D geometries directly from raw materials, which require little follow-on post-processing [53]. In this work, three most popular powder-based high energy AM methods -DED, SLM and EBM- that are used to produce dense structures through melting and solidification, are considered because the objective is to produce dense Ti6Al4V products for load-bearing applications. It needs to be noted that in addition to powders, wire-type materials can also be used as feedstock materials, and wire-based AM methods such as wire arc additive manufacturing is gaining significant attention in additive manufacturing of Ti6Al4V alloys [54–56]. However, this review work attempts to make a consistent comparison and hence only focuses on the powder-based AM processes with commonly used DED, SLM and EBM.

The common feature of these AM processes is the utilization of geometrical data contained in a 3D computer aided design (CAD) file, which is sliced into layers with a defined thickness. Following the sliced pattern, a focused, high power laser or electron beam scans and melts the precursor powders, forming a molten pool. As the heating source moves away, the molten pool cools down quickly and solidifies to form a track bead. This process is repeated to successively build new layers until a final geometry is completed. Among the three techniques, DED is a blown powder method as metallic powders are delivered by continuous feeding through nozzles, while SLM and EBM are both powder bed fusion processes where the individually preplaced powder layers are selectively melted. The working principles for DED, SLM and EBM are schematically illustrated in Fig. 2.

During a DED process, the laser beam creates a molten pool, into which the powder material is delivered via argon gas and locally injected to fuse and solidify into a bead [59]. After building one layer, the laser and powder feeding head is raised in Z direction with a preset height and start building a subsequent layer [38]. The DED process is usually conducted in an inert environment filled with the argon gas where the oxygen level can be controlled to below 5–10 ppm. After deposition, the unused blown out powders can be recycled [30].

Due to the nature of the DED process, a high degree of control and process capability is possible. Compared with powder bed techniques, DED has a higher degree of freedom in composition design as it can simultaneously feed different kinds of powders through multiple hoppers; therefore, DED is applicable to building composite materials or compositionally graded materials [40,60,61] (Fig. 3). In addition, the DED process is ideally suited to enhancing and repairing high-valued metal components because it is capable of accurately adding materials onto worn or damaged areas with minimum waste [59,62–64]. This capability enables DED to repair thin-walled components such as gas turbine blisks [65] and turbine blades [57] (Fig. 4). The repaired parts usually have equivalent or even better mechanical properties than initial parts [66].

SLM started in 1995 at the Fraunhofer Institute ILT [67]. The predominant difference between DED and SLM is the way to feed powder materials. In SLM, metallic powders are uniformly spread on the building platform by a rake instead of being blown out from nozzles as in DED. A focused laser beam scans the surface according to the prescribed path and selectively melts the powders in this layer, after which a new layer of powders is spread after lowering the building platform to the distance of the layer thickness. The layer height of SLM is in the scale of tens of microns, which is much thinner than that of DED and EBM products [58]. The non-melted powders are left in the powder bed to support the subsequent layers. Powders surrounding the deposited parts are affected by the thermal process and cannot be reused due to the change of physical properties.

EBM was proposed and commercialized by Arcam AB in 2001 [68]. Similar to SLM, EBM is also a powder bed fusion process, but its heating source is an electron beam instead of a laser beam. Because of the special working nature of electron beam, EBM builds parts in a high-vacuum environment of 10^{-4} mbar or greater, providing an ideal contamination-free environment for manufacturing of reactive materials that have a high affinity to oxygen and nitrogen, such as Ti6Al4V. Additionally, EBM generates a faster build rate than DED and SLM due to its superior energy input and fast scan speed [69]. The shortcoming is its inferior surface quality. The high build temperature of 600–750 °C also leads to different manufacturing features (will be discussed in the following sections). Table 1 summarizes the main parameters of Optomec 750, Realizer SLM50 and Arcam EBM S12, which are common machines in DED, SLM and EBM processes, respectively.

2.2. Thermal behavior

AM processes involve complex multi-physics, non-equilibrium phenomena, which are affected by a group of process parameters, such as power, scan speed, scan strategy, layer height, hatch spacing, etc. Powder bed and blown powder AM processes are distinguished by remarkable differences in energy input and thermal behaviors. Interaction between a laser/electron beam and precursor powders also relies on powders' absorptivity, physical properties as well as particle sizes and shapes. Under these circumstances, the approximate input energy density E (in J/m^3) is used to provide a basic starting point for comparison between different AM processes. E is the absorbed energy density and has the expression as:

$$E = \frac{\alpha P}{\nu \cdot h \cdot t} \tag{1}$$

where P is the power (in J/s), ν is the scan speed (in m/s), h is the hatch spacing (in m), t is the layer thickness (in m) and α is the

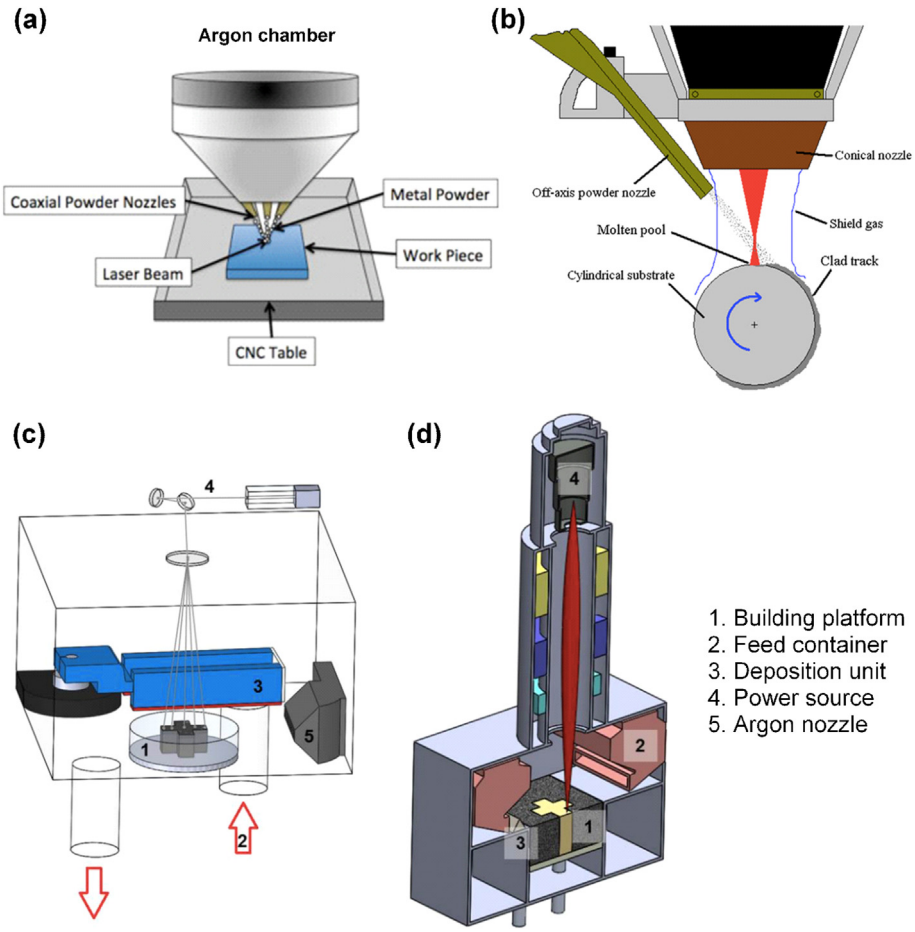

Fig. 2. Working principles of: (a) Directed energy deposition. Reproduced with permission from Elsevier [57]. (b) Directed energy deposition on a tube substrate, also known as laser cladding. Reproduced with permission from Springer Nature [38]. (c) Selective laser melting [58]. (d) Electron beam melting [58].

absorptivity. In the DED process, heat dissipates from the molten pool via conduction downwards as well as forced convection by the shielding gas flows [73]. SLM, on the other hand, typically relies on conduction through the unmelted powders surrounding the part to dissipate heat [73]. Similar to SLM, the components fabricated using EBM are also surrounded by partly melted metallic powders, and thus conduction dominates the heat transfer in the EBM process. Heat loss via radiation also plays a role but can be neglected as compared to conduction.

Due to the highly concentrated energy source and extremely short interaction time, a high temperature and cooling rate will be produced in the molten pool. For example, Qian et al. [74] reported a cooling rate of approximately 7×10^4 K/s in DED of Ti6Al4V. Yu et al. [75] also reported a cooling rate of around 10^6 K/min. Similar to the DED process, Yadroitsev et al. [76] reported a maximum temperature of about 2710 K in the Ti6Al4V molten pool created by SLM, which also produces a cooling rate in the range of about 10^4–10^6 K/s [77,78].

In order to precisely understand the thermal behavior of AM processes, the authors' group developed a laser direct deposition model to analyze the temperature history for a three-track laser direct deposited Ti6Al4V (Fig. 5). The model considers laser-powder interaction, mass addition, heat transfer and fluid dynamics in the molten pool occurring in the laser direct deposition process. Actual deposition parameters and temperature-dependent material properties were used as inputs in the model. Fig. 5 illustrates the extracted free surface, molten pool and heat affected zone boundaries that are superposed on the experimental micrograph, which show an excellent agreement. The temporal and spatial temperature fields in the molten pool generated at eleven different locations along the dashed line on the micrograph are also shown. A maximum temperature of approximate 2600 K is

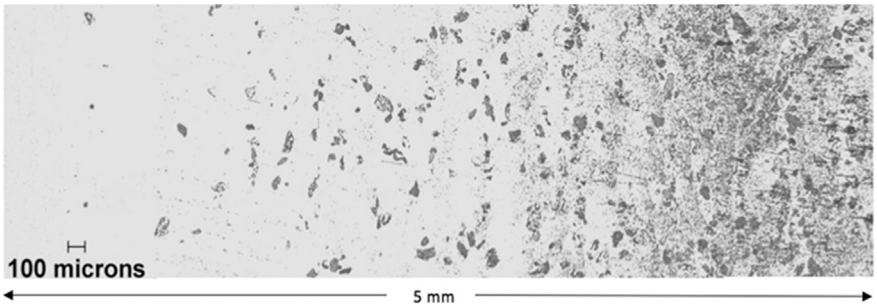

Fig. 3. Laser direct deposited (directed energy deposited) functionally graded Ti64-TiC composite with (0–40) vol% TiC. Reproduced with permission from Elsevier [61].

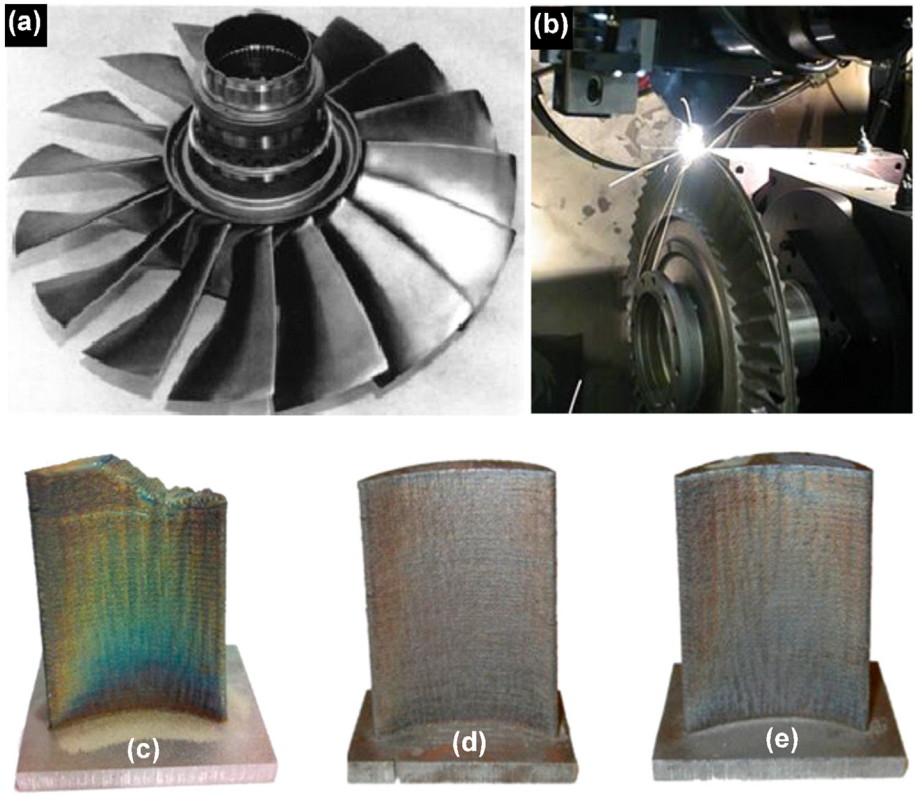

Fig. 4. Damaged blisk repaired using directed energy deposition process: (a) repaired blisk, (b) repairing in process [65]; damaged turbine blade repaired with directed energy deposition: (c) damaged blade, (d) original undamaged blade, (e) repaired bladed. Reproduced with permission from Elsevier [57].

generated in the molten pool and it decreases to room temperature within about 0.25 s as the laser beam moves away. The average cooling rate in the molten pool is about 10^4 K/s, and even in the heat affected zone an average cooling rate of about 5×10^3 K/s is still obtained. As the laser scan speed for this deposition is 15 mm/s, even for scanning a small layer of 1 cm^2, the temperature has dropped to near room temperature before the laser travels back to the same location for the subsequent layer.

As for the EBM process, the temperature in the molten pool was estimated to be between 1900 °C and 2700 °C [79,80]. Price et al. [81] conducted a specific study using thermography and measured a temperature of 2500 °C in the molten pool. Al-Bermani et al. [82] calculated the cooling rate of an EBM fabricated Ti6Al4V bead on a stainless steel substrate and obtained a cooling rate between 10^3 and 10^5 K/s. Antonysamy et al. [83] also obtained a cooling rate in the order of 10^4 K/s through simulation. Although the cooling rate in EBM fabricated Ti6Al4V is in a similar scale to those of DED and SLM, the thermal behavior of EBM built parts is different since it has a high build temperature in the range of 600 to 750 °C [70–72]. This high build temperature behaves like a post heat treatment process. The resultant parts are hence different in microstructure and material properties, as will be discussed in Sections 3 and 4.

2.3. Defects and residual stresses

All AM processes have intrinsic limitations, including the risk of porosity, presence of surface roughness, high affinity to oxygen and high tensile residual stresses. These restrictions impose a severe detrimental effect on the mechanical performances of as-built components. In this section, the defects formed in AM Ti6Al4V parts are discussed.

2.3.1. Porosity

AM techniques can in theory produce a fully dense structure, but non-optimal deposition parameters will result in porosity. Controlled porous structures have been used to tailor the mechanical properties. For Ti6Al4V, such applications using the pores include those to address the “stress shielding effect” in load-bearing implants and to attenuate the impacts [10,12,84–86]. However, the uncontrolled pores in AM fabricated Ti6Al4V will deteriorate the material properties. Vilaro et al. [87] observed that the pore shape and orientation strongly influence macroscopic ductility. Biswas et al.'s [43] and Li et al.'s [88] macroscopic experiments and microstructure analysis revealed that the pores are likely to become the nucleation sites for adiabatic shear bands and microcracks.

Table 1
A comparison between Optomec 750 (DED), Realizer SLM50 (SLM) [58] and Arcam EBM S12 (EBM) [58].

Feature	Optomec 750	Realizer SLM50	Arcam EBM S12
Heating source	Laser	Laser	Electron beam
Environment	Argon	Argon	Vacuum (10^{-4}–10^{-5} mbar)
Powder feed	Blown powder	Powder bed	Powder bed
Preheating, °C	–	200 (building table resistive heating)	600–750 (powder bed heating by an electron beam) [70–72]
Maximum beam power, W	500	120	3500
Beam spot, μm	660–900	30–250	200–1000
Scan speed, m/s	0.001–0.04	0.3–1	>1000
Layer thickness, μm	200–1000	20–100	50–200

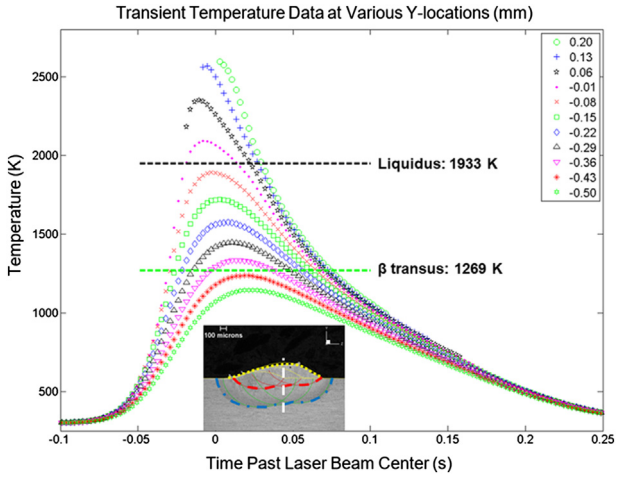

Fig. 5. The temporal and spatial temperature fields in the molten pool generated at eleven different locations along the dashed line on the micrograph of three-track laser direct deposited Ti6Al4V, where the extracted free surface (yellow line), molten pool (red line) and heat affected zone (green line) boundaries are superposed.

Uncontrolled porosity is actually very common in AM parts. Leuders et al. [47] detected a porosity of 0.23% in SLM specimens using the X-ray tomography. Kasperovich and Hausmann [48] reported that the porosity of 0.08% can still remain under optimized SLM parameters, and the pores with a small size occupy a substantial volume percentage. Porosity has also been characterized in EBM specimens. Ackelid and Svensson [89] found a porosity of 0.17% in as-built EBM parts. The pore size was known to range from 50 μm to 300 μm [90–92]. The authors built dense Ti6Al4V parts using a DED process with optimized parameters. The X-ray tomography examination of these dense parts revealed the porosity of only about 0.1%, and the pores are about 1–3 μm in diameter (Fig. 6). In order to get rid of pores, the as-built AM parts are commonly subjected to post-processing. However, heat treatment cannot bring the closure of pores [47]. Only HIP was found to have a positive effect on the reduction of porosity [45–48]. For example, the pore volume fraction was decreased from 0.08% to 0.01% after HIP [48], and the size of pores were also dramatically reduced [47].

Two types of pores prevail in AM manufactured products: gas pores and lack-of-fusion pores [88]. Fig. 7 illustrates the morphology of these two pores. Gas pores usually exhibit a spherical or elliptic shape with a diameter of about 1–100 μm, and are randomly distributed in the material (Fig. 7(b)). The round shape of these pores indicates that they are formed due to the gas entrapment such that the gas trapped in the molten pool did not escape in time and was hence stuck in the solidified bead [93–95]. Therefore, dense metal powders are preferred to sponge type powders as feedstock materials in AM processes because the hollow structure in sponge powders easily introduces gas pores [96,97]. Usually, slowing down the scan speed and increasing the laser power will alleviate the formation of gas pores to some extent but can hardly eliminate them thoroughly [95,98].

Different from gas pores, lack-of-fusion pores tend to be larger and display an irregular-wedge shape or band shape with sharp tips at two ends (Fig. 7(a)). These pores are generally distributed at the boundary zone of two adjacent layers, leaving thin interface flat cracks. As described in literature [41,87,99,100], the lack-of-fusion pores are mainly produced because of deviation from optimal melting conditions, such as the insufficient laser energy trying to melt an excessive amount of powders, which results in inadequate melting and weak bonding between layers. The short axis of lack-of-fusion pores is typically aligned in the building direction. When exposed to loading, particularly under the uniaxial tensile load parallel to the building direction, the sharp tips of these pores are prone to concentrated local stresses, leading to premature failure [87,88]. Compared to gas pores, lack-of-fusion pores more fatally affect the performance of AM manufactured products, but are considered as avoidable [45]. An effective way to reduce lack-of-fusion pores is to increase the input energy density according to Eq. (1).

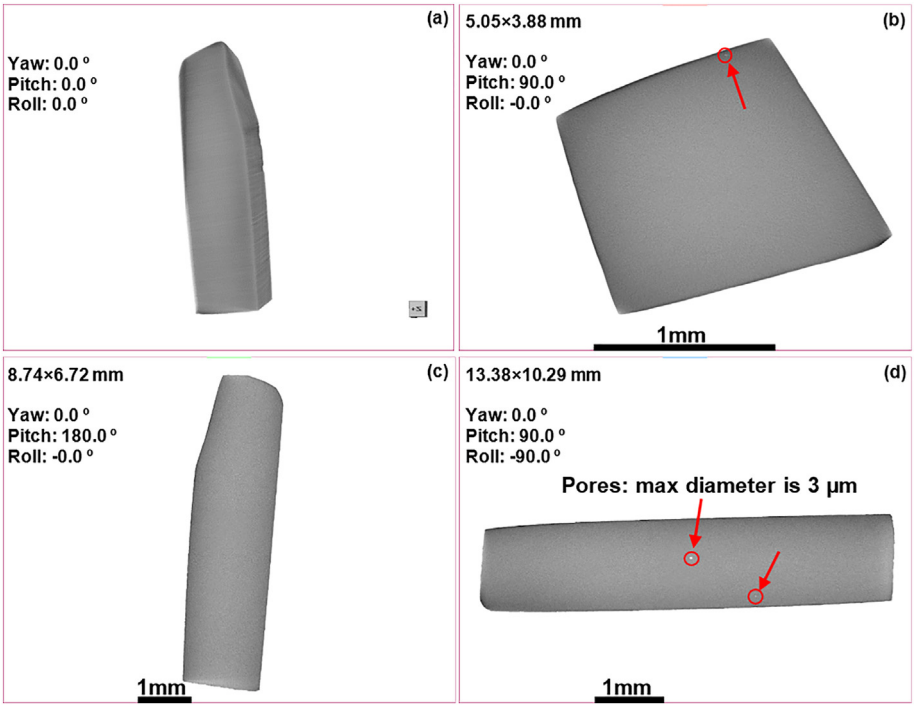

Fig. 6. X-ray tomography examination of laser direct deposited dense Ti6Al4V part with an overall view in (a) and slice views in (b, c, d) reveals a porosity of about 0.1% and pores with a diameter in the range of 1–3 μm. The pores were circled and indicated by the red arrows.

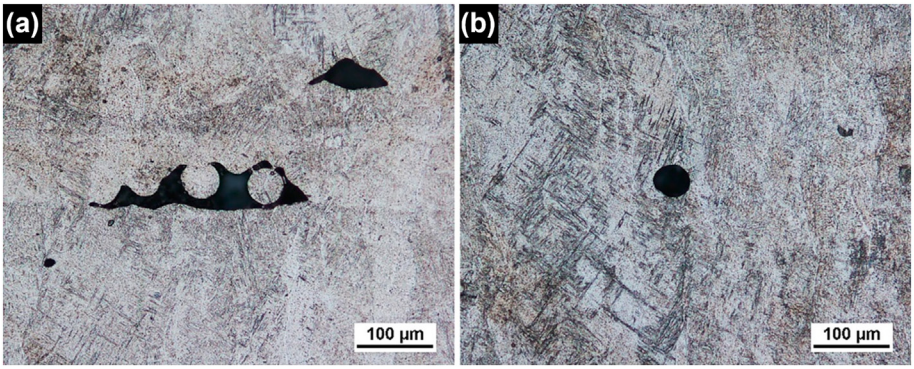

Fig. 7. Porosity in electron beam melting of Ti6Al4V: (a) lack-of-fusion pore and (b) gas pore. Reproduced with permission from Elsevier [93].

2.3.2. As-built surface roughness

Another limitation of AM processes is the high surface roughness of as-built components [101]. Some reported surface roughness values for different AM processes are included in Table 2. DED produces the smoothest surface finish, followed by SLM and EBM processes. Li et al. [102] pointed out that oxidation and the adhesion of partially melted particles on the part surface are the most important factors that determine the surface quality. As DED process blows away the unused powders while SLM and EBM methods keep the unused powders in the powder bed, adhesion of partially melted powders is less for the DED process as compared to SLM and EBM methods.

Comparing the surface roughness between SLM and EBM built Ti6Al4V parts, Rafi et al. [103] concluded that the different scan speeds, powder sizes and layer heights should be responsible for the different surface roughness. Fig. 8 shows the external surface morphologies of vertically and horizontally built Ti6Al4V specimens by SLM and EBM. As clearly shown, the EBM built surface has more partially melted powders adhered while the SLM built surface is much smoother. This should be attributed to the higher thermal radiation induced by the high-energy electron beam. As for the horizontally built parts, the curved surface formed by consecutive steps in the EBM process (Fig. 8(d)) displays a more "waving" pattern as compared to that of SLM built specimens (Fig. 8(b)). As the stairstep effect is associated with the track width and hatch spacing (the distance between adjacent tracks), EBM apparently creates a wider molten pool, which is detrimental to creating a smooth surface. In addition, the surface roughness value of EBM parts is very close to the particle size of the precursor powders; therefore, finer powders would improve the surface quality of EBM parts.

Li et al. [69] summarized three reasons for the formation of surface roughness: (1) the staircase effect related to the increased layer number, (2) the adherence of partially melted powders to the external surface, and (3) the existence of open pores and incompletely melted regions. Actually, surface roughness varies with processing parameters. For example, Resch et al. [111] showed that surface roughness decreases with a decrease in powder feed rate but an increase in scan speed. Zhai et al. [72] measured the areal surface roughness of Ti6Al4V parts built by DED and EBM and observed that higher laser power in the DED process yields a higher surface roughness. An opposite experimental result was however revealed in Mahamood and Akinlabi's work [105], who experimentally proved that increased laser power decreases the roughness of DED manufactured Ti6Al4V. In addition, a proper set of hatching spacing values will effectively flatten the surface. For example, Kaplan and Groboth [112] found that a larger overlap decreases the surface roughness, which is consistent with the findings of Mazumder et al. [113].

However, it should be noted that the optimization of deposition parameters can only alleviate the surface roughness problem to a limited extent. The most effective method to decrease the surface roughness is to polish the surface. Formanoir et al. [99] showed that polished specimens exhibit higher strain to failure than as-built specimens. This results from the mechanical removal of critical defects at the surface, which induce stress concentration and act as crack initiators. In actual applications, nearly all AM parts will require some type of post-processing to smooth the surface, such as machining for simple structures [27,99], and chemical etching and vibrahoning for complex geometries [114].

2.3.3. Residual stresses

AM processes, particularly the laser-based AM processes, are prone to a significant amount of induced residual stresses because of their inherent large temperature gradients [16,115–117], which are normally in the order of ~5×10^4 K/cm in beam-based additive manufacturing of Ti6Al4V [118]. The final residual stresses will increase with increased layer numbers [119], and the peak value always occurs at or near the free surface of the final deposited layer [108,115,120]. Mercelis and Kruth [119] claimed that the residual stress profile is made up of a large amount of tensile stresses at the top region of the part, whose value is up to the part's yield strength. With addition of new layers on the previously built layers, the tensile stress converts into compressive stresses due to subsequent thermal cycling [120]. The deposition strategy and track length also have a large influence on residual stress levels. Researchers have observed that residual stresses are larger along the scan direction than the perpendicular direction due to the larger thermal gradient along the scan direction [16], creating an anisotropic stress distribution in the final part [16,120]. Moreover, residual stresses also increase with the scan length [119,120].

It is well known that residual stresses contribute to the crack formation and warping in the part, leading to the disconnection of builds from the substrate and cracks in the finished parts [119,120]. Fig. 9 shows the typical failures caused by the concentrated tensile residual stresses. These failures will always cause immediate and fatal consequences of impairing the geometrical accuracy and destroying the structures

Table 2
Quantified porosity, surface roughness and residual stresses in as-built Ti6Al4V parts fabricated by directed energy deposition (DED), selective laser melting (SLM) and electron beam melting (EBM) processes.

AM process	Porosity (vol%)	Profile surface roughness, Ra (μm)	Areal surface roughness, Sa (μm)	Residual stresses, σ (MPa)
DED	0.01–0.27 [94]	0.24–13.3 [104,105]	30.6–63.9 [72]	–
SLM	0.1–0.5 [106,107]	5–40 [108,109]	–	100–500 [110]
EBM	0.1–0.3 [41,106]	25–131 [109]	45.7 [72]	Very low [110]

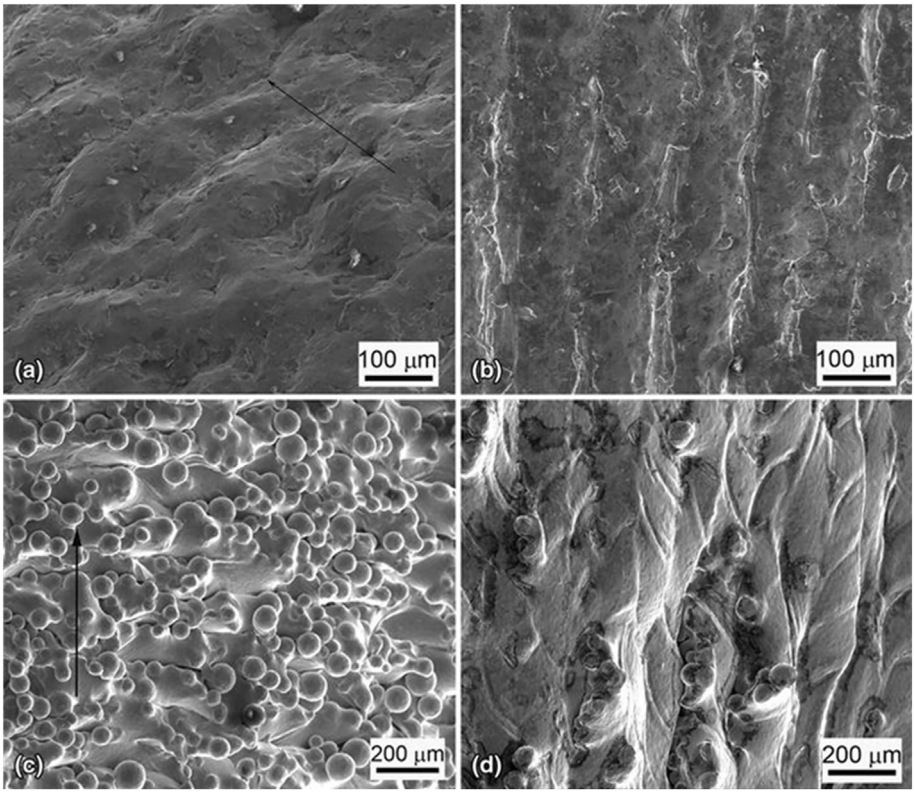

Fig. 8. External surface morphology of (a) a longitudinally built SLM specimen, (b) a horizontally built SLM specimen, (c) a longitudinally built EBM specimen, (d) a horizontally built EBM specimen. For longitudinal samples, the arrow shows the building direction while for the horizontal samples, building direction is perpendicular to the image plane. Reproduced with permission from Springer Nature [103].

durability. Therefore, SLM and EBM built parts may require supporting structures to restrict bending or distortion during manufacture [121,122].

As residual stresses originate from thermal gradients, a way to relieve them is to decrease the thermal gradient by using a high temperature stress relief heat treatment. Vastola et al. [115] systematically calculated the residual stresses formed in the single-track EBM Ti6Al4V by varying the pre-heating temperature of the fusion bed, and found that the bed pre-heating temperature has the most significant impact on the residual stress. Quantitatively, each increment by 50 °C in pre-heating temperature shows a stress reduction by about 20%. As introduced in Section 2, the EBM process maintains a build temperature of 600–750 °C throughout the deposition [70–72]. Generally, it takes about 5 h to achieve a complete stress relief at this temperature while EBM deposition cycles mostly run longer than 5 h. Therefore, contrary to the DED and SLM processes, it is widely accepted that residual stresses can be negligible in the EBM process. For example, Hrabe et al. [45] utilized neutron scattering to measure residual stresses in EBM Ti6Al4V parts and did not measure a significant level of residual stresses. Chastand et al. [71] performed stress relief annealing at 640 °C for 4 h for the SLM built Ti6Al4V specimens before a fatigue test but not for the EBM built parts because the EBM building chamber was maintained at 680 °C.

3. Microstructures of AM manufactured Ti6Al4V

Microstructure refers to phases and grain structures present in a metallic component. Microstructure directly governs the material properties of final products but is determined by the manufacturing processes used. In this section, the as-built microstructures of DED, SLM and EBM manufactured Ti6Al4V are comparatively assessed with a focus on phase formation and grain coarsening.

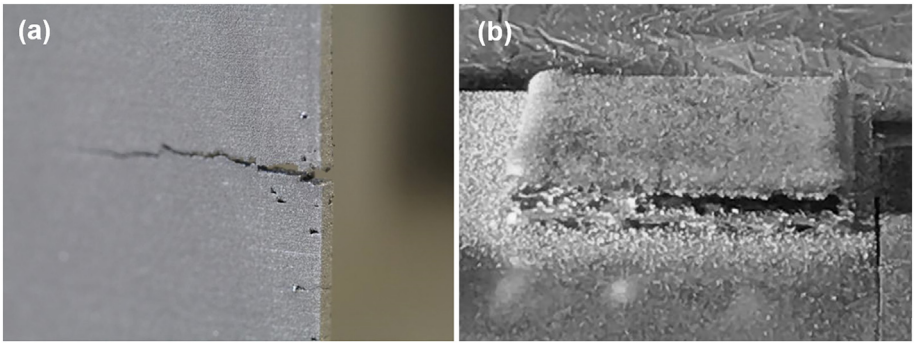

Fig. 9. (a) Crack formation induced by the build-up of residual stresses during manufacturing of a Ti6Al4V component. Reproduced with permission from Elsevier [16]. (b) Disconnection of parts from substrate plate caused by the accumulation of residual stresses.

3.1. Phases

3.1.1. Phase transformation

Ti6Al4V is a titanium alloy that solutes 6 wt% Al and 4 wt% V to pure Ti. Ti is an allotropic element that exists in two different crystal structures: α-Ti with Ti atoms arranged in a hexagonal close-packed (HCP) array exists below the β transus temperature while body-centered cubic (bcc) β-Ti exists above the β transus temperature. As Al is an α stabilizer while V stabilizes β, Ti6Al4V maintains α + β dual-phase at room temperature. However, the phase transformation in Ti6Al4V strongly depends on the temperature history and cooling rates induced by the fabrication process [123]. α + β dual phase only exists in slow solidification processes. Upon fast cooling from above the β transus temperature, β will be decomposed by a non-equilibrium martensite reaction instead of α + β transformation. The formation of alpha prime (α′) martensite phase is beneficially produced by the rapid cooling through diffusionless transformation while α + β transformation is a diffusional process.

Yang et al. [124] claimed that the microstructure of SLM Ti6Al4V consists of four different martensites: primary, secondary, tertiary and quartic α′ martensites, which contain a large amount of dislocations and twins. The size of these martensites can be controlled by adjusting the SLM processing parameters [124], which varies in the size of minor axes from 1 to 3 μm for primary [48,58,124–126] and secondary α′ to shorter than 20 nm for quartic α′ [124,125]. After cooling to room temperature, some β can still be detected due to the fact that the finishing temperature of martensite transformation (M_f) for Ti6Al4V is below room temperature.

Fig. 10 shows the phase diagram of Ti6Al4V alloy [127]. In the complete melting and solidification case, Ti6Al4V experiences α + β → β → liquid→β → α + β/α′ phase transformation. The formation of α′ martensite requires a specific thermal history. Only sufficient cooling rates along with build temperatures lower than the martensite start temperature (M_s) can lead to the formation of α′ martensite (Fig. 10). A variety of M_s temperatures have been reported for Ti6Al4V, ranging from 575 °C [128] to 800 °C [129,130] because the initial microstructure, composition homogeneity and impurity elements are known to affect the M_s temperature [129,131]. This situation also works for the β transus temperature, as shown in Fig. 10. α′ martensite forms within a specific cooling rate range [128]. The regions in which the cooling rate exceeds 410 °C/s will produce a complete α′ martensite, while the cooling rate between 410 °C/s and 20 °C/s will lead to incomplete transformation to α′ phase, and the cooling rate that is <20 °C/s will not produce α′ [128].

According to the thermal behaviors of AM processes discussed in Section 2.2, α′ martensite is expected to dominate the as-built microstructure of AM fabricated Ti6Al4V parts. Fig. 11 shows the optical micrographs of final α/α′ microstructures within prior β grains in DED, SLM and EBM manufactured Ti6Al4V components. Microstructures produced by several typical manufacturing methods are also presented in Fig. 11(d–f) for comparison. A higher magnification TEM result is given in Fig. 12 to illustrate the grain size of different phases produced in EBM and SLM Ti6Al4V. In an optical micrograph, α and α′ phases are bright while β phase is dark. The as-built microstructures of DED and SLM Ti6Al4V specimens are definitely dominated by the fine needle-shaped α′ martensite, with a typical lath width about 0.2–1 μm, (Fig. 11(a, b) and Fig. 12(b)). The presence of α′ was confirmed by the X-ray diffraction pattern, which reveals the α′ phase with the hexagonal lattice of a = 0.293 nm and c = 0.467–0.0468 nm [75]. Different from DED and SLM, EBM produces an α + β dual phase, where the α-lath has an average length and thickness of 1–3 μm and 0.5–1 μm, respectively while β platelets are about 0.1 μm thick (Figs. 11(c) and 12(a)). Al-Bermani et al. [82] also detected some α′ martensite mixed with α phase but α′ mainly existed in small parts or within several hundred microns from the top surface of a large component where the cooling rate is high.

As seen in Fig. 11(c) and (d), EBM Ti6Al4V shows a similar microstructure to that of annealing condition but quite different from those built with DED and SLM. This is also confirmed by Koike et al.'s work [132] as well as Hrabe and Quinn's work [133], where EBM built Ti6Al4V has an α-lath thickness of about 1 μm, equal to that of SLM Ti6Al4V subjected to heat treatment at the EBM's chamber temperature [48,126]. This difference in microstructure is associated with the different thermal histories. As introduced in Section 2, the predominant difference that distinguishes EBM from DED and SLM is its high build temperature. This high build temperature has a substantial effect on microstructure evolution because it provides the in-process heat treatment of α′ martensite and decomposes α′ to the equilibrium α + β microstructure [58,72,79,93,132]. Taking advantage of the high build temperature and low cooling rate, even as-built SLM Ti6Al4V can produce an α + β dual phase instead of α′. This possibility has been confirmed by Simonelli et al. [134]. The authors used a low laser power and low scan speed to enable a long laser-material interaction time and high energy input, which provided high temperature in the deposition, long time for composition diffusion and also reduced the cooling rate. As a result, an α + β microstructure was successfully obtained in the as-built SLM Ti6Al4V part.

As shown in Fig. 10(b), the phase transformation in EBM Ti6Al4V can generally be simplified to three main stages according to the EBM's thermal behavior [31,79,136]. In the first stage, the molten pool cools rapidly from the peak temperature to the build temperature under a high cooling rate. In this stage, a diffusionless martensitic transformation occurs. The second stage can be considered as a quasi-isothermal annealing stage as the part is held at the build temperature (about 600–750 °C) until the completion of deposition [72,93,103], where the metastable α′ is decomposed to α + β structure [31,58,72,79,93,132,136]. The temperature-dependent decomposition of α′ has been investigated by Gil Mur et al. [130] via heat treatments

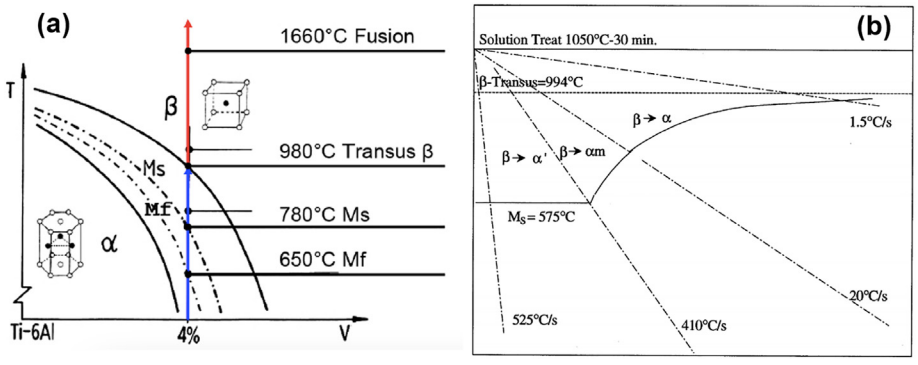

Fig. 10. (a) Phase diagram of Ti6Al4V. Reproduced with permission from Springer Nature [127]. (b) Phase transformation as a function of cooling rates. Reproduced with permission from Elsevier [128].

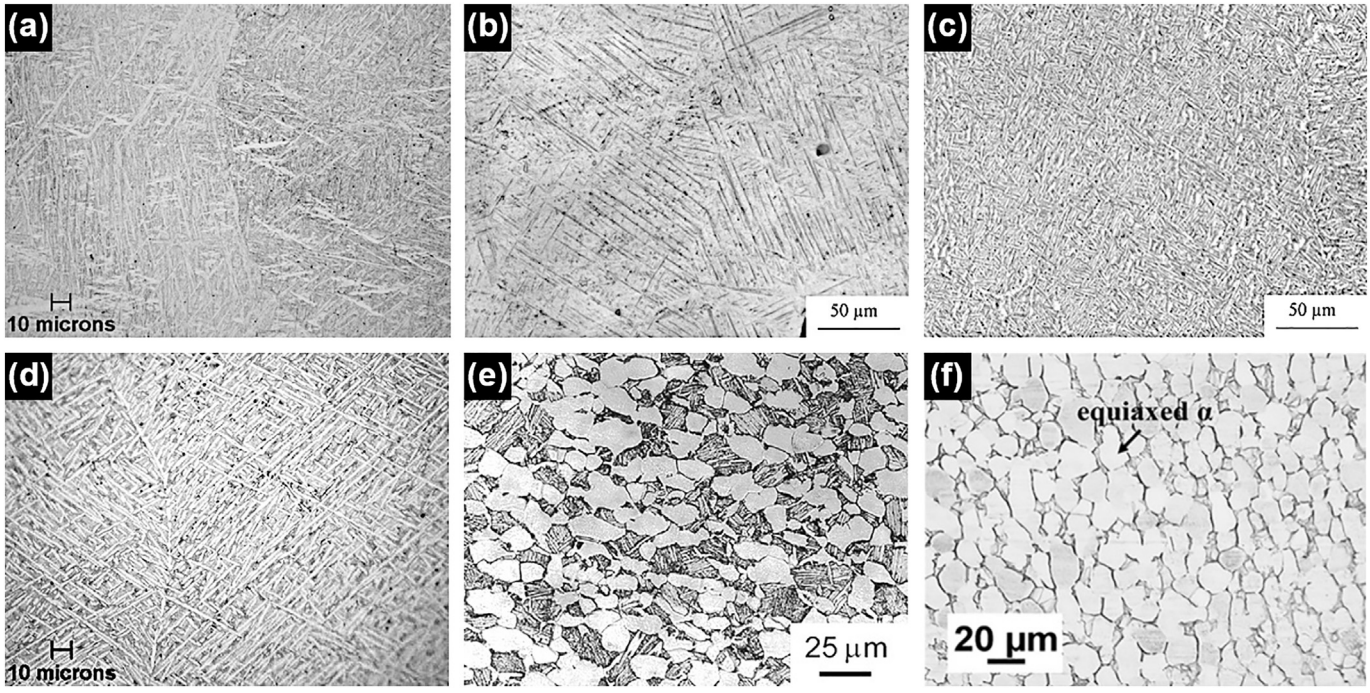

Fig. 11. Optical microstructures of Ti6Al4V built with different fabricating methods: (a) Directed energy deposited Ti6Al4V produces acicular α′ martensite phase. (b) Selective laser melted Ti6Al4V microstructures also reveals α′ martensite. Reproduced with permission from Springer Nature [10]. (c) Electron beam melted Ti6Al4V has a fine α + β dual phase. Reproduced with permission from Springer Nature [10]. (d) Annealed microstructure (940 °C/1 h/air cooling) of directed energy deposited Ti6Al4V shows an α + β dual phase. (e) Solution treated and overaged microstructure of wrought Ti6Al4V reveals an equiaxial prime α and secondary α + β lamellae. Reproduced with permission from Springer Nature [135]. (f) Mill-annealed Ti6Al4V presents equiaxial α colony. Reproduced with permission from Elsevier [72].

from 400 °C to 800 °C. The results showed that the temperature higher than 700 °C can result in a complete decomposition of α′, while below 600 °C it only results in an incomplete decomposition of α′ martensite. Therefore, a complete α + β or a mixture of α + β/α′ will be obtained after this stage depending on the build temperature. In the last stage, the temperature drops slowly from the build temperature to room temperature, which will not lead to any phase transformation [48,101].

3.1.2. Phase prediction

Section 3.1.2 qualitatively illustrates the phase transformation in DED, SLM and EBM built Ti6Al4V components. Actually, the volume fraction of α′ in the final microstructure can be quantitatively calculated as a function of temperature and cooling rate. Compared with grain size, phase plays a more dominant role in determination of the final material properties. If the phase can be accurately predicted, the material properties can also be predicted, which saves the vast amount of experimental studies. The authors' group has developed a phase prediction model to predict the phase transformation in DED manufactured Ti6Al4V [137]. The details of the model and the predicted microstructure as well as the corresponding microhardness are presented. Even though the model was developed focusing on the DED process, it can be applied to SLM and EBM processes as long as the temperature field is known.

The temperature history produced by the DED thermal model (Fig. 5) is used to conduct the simulation. The cooling rate is calculated based on the temperature field as:

$$\dot{T} = \frac{dT}{dx}\frac{dx_{laser}}{dt} \tag{2}$$

where T is temperature and $\dot{T}$ represents the local cooling rate.

The intermediate volume fraction of α′ is a function of cooling rate as:

$$\alpha'_{fi} = \left(\frac{\dot{T}-20}{390}\right)\left(\tag{3}$$

where α'_{fi} is the intermediate partial phase transformation between the complete and zero α′ transformation at cooling rates of 410 °C/s and 20 °C/s, respectively. The produced volume fraction of α′ martensite (α'_f) is calculated by multiplying α'_{fi} with the volume fraction of transformed β

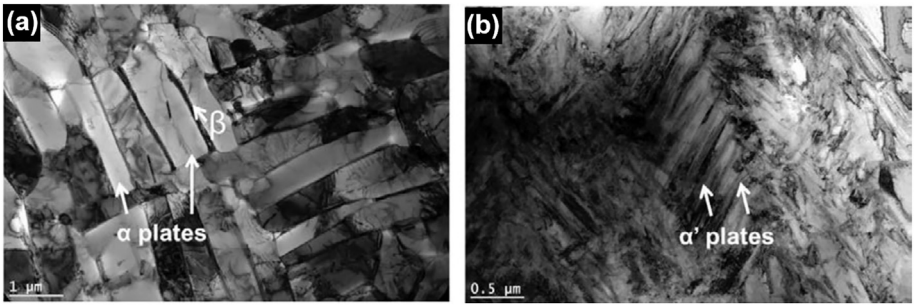

Fig. 12. TEM micrographs of (a) EBM and (b) SLM fabricated Ti6Al4V [58].

phase, β_n as:

$$\alpha'_f = \beta_n \cdot \alpha'_{fi} \tag{4}$$

where β_n is only calculated in regions where the highest temperature is between the β transus temperature and the liquidus temperature. The detailed expression of β_n can be found in Ref. [137].

As the volume fraction of α'_f is calculated, the volume fraction of formed α phase is $1 - \alpha'_f$. The final microhardness of the AM parts can be hence calculated by the rule of mixtures, as shown in Eq. (5):

$$H = \alpha'_f H_{\alpha'} + \left(1 - \alpha'_f\right) H_{\alpha} \tag{5}$$

where H_α and $H_{\alpha'}$ are the hardness values of α phase (30 HRC) and α′ phase (44 HRC), respectively [138]. Using Eq. (5), the prediction of α′ fraction can be validated.

Fig. 13 shows the predicted microhardness along two parallel dashed lines compared to experimental measurements. The two lines were separated by a distance of 200 μm, with the upper line encompassing the fusion zone and heat affected zone and the bottom line only encompassing the heat affected zone. As shown in Fig. 13, the overall microhardness prediction is in excellent agreement with experimental results. A constant peak microhardness value of 427 $HV_{0.2}$ is obtained in the fusion zone and the shape of fusion zone identified by this maximum microhardness matches the microstructure observation, indicating a complete formation of α′ martensite in the molten pool. After building multi-layers, the whole bulk structure will consist of α′ martensite, which matches the microstructure illustrated in Fig. 11(a).

3.2. Grains

3.2.1. Prior β grains

As discussed in Section 3.1, on solidification of the molten pool the melt will first be transformed to prior β phase when the temperature approaches the solidus temperature, and then α/α′ phases are formed within prior β grains when the temperature drops below the β transus. The size, shape and distribution of parent β grains will definitely affect the morphology of α/α′ phases [139] as well as the material performance. In all AM manufactured Ti6Al4V samples, columnar β-grain structures are found to dominate the microstructure.

In attempts to uncover the growth mechanism of β grains in AM built Ti4Al4V parts, comprehensive research has been conducted to reconstruct the primary β-grain structure and texture based on the electron back scatter diffraction data. These studies demonstrate a strong $\langle 001 \rangle_\beta$//Nz fiber texture of prior β grains with the longitudinal axis parallel to the building direction in EBM Ti6Al4V [82,83]. A similar texture feature of β grains is also observed in SLM fabricated Ti6Al4V [42,51,140,141] and DED built components [75,142–144]. Wu et al.

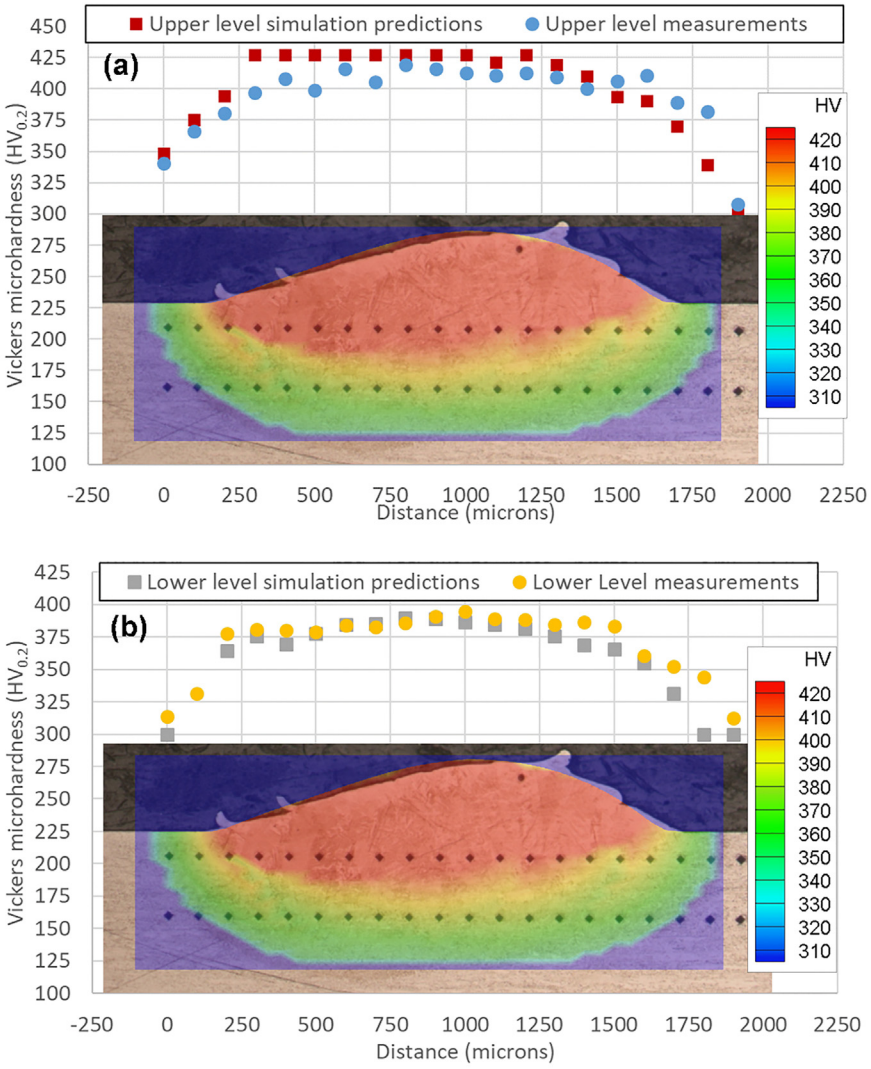

Fig. 13. Microhardness prediction for three-track laser direct deposited Ti6Al4V compared to experimental measurements: (a) upper level measurements and (b) lower level measurements.

[142] investigated the effects of DED parameters on the microstructure evolution. The long columnar β grains were found to form for all conditions except for very high laser power, and the scale of these grains increased with a decrease of laser scan speed when other parameters were the same. Antonysamy et al. [83] studied the influence of component shape on the microstructure and texture of β grains by building various structures using EBM. Only the grains that grew near the substrate or limited by the thickness of the part exhibited a dominant cubic and 45° rotated cubic morphology [82,83]. Otherwise, the prior β grains grew predominantly aligning with the $\langle 001\rangle_\beta$//Nz direction and were free from fabricated geometries [83].

Fig. 14 presents the typical as-built morphology of primary β-grain structure formed in DED, SLM and EBM manufactured Ti6Al4V components. All these microstructures feature columnar β grains extending over multilayer cross-sections. The size of β grains varies from 1 to 20 mm in length and from 0.2 to 4 mm in width [142,144]. These β grains are obviously far taller than the layer thickness. Apparently, the epitaxial growth must have taken place through nucleation onto the top surface of previous layer via re-melting and resolidification processes. Layer bands are observed in Fig. 14(a), which are formed due to the microstructure coarsening in the re-melted region of previous layers. These layer bands characterize a layer-by-layer deposition pattern of AM processes but are prone to being formed in the area where heat extraction is fast, such as the region near the substrate [142].

Theoretically, the growth of a grain should go opposite to the maximum temperature gradient at the solidification front [145]. β phase has a BCC lattice structure, whose preferential growth direction is $\langle 001\rangle_\beta$. Under the condition of directional solidification, the β grain should grow along the preferred $\langle 001\rangle_\beta$ orientation. As the $\langle 001\rangle_\beta$ direction is generally parallel to the building direction, the overall heat flow direction in AM processes is believed to be perpendicular to the substrate, which is caused by the conductive heat flow downward and convective heat transfer outward. However, as illustrated in Fig. 14, the $\langle 001\rangle_\beta$ axis actually is tilted from Nz to some extent with small angle oscillations, which indicates the complexity in AM's thermal behavior. AM processes are known to be track-by-track and layer-by-layer techniques. Heat dissipation from a molten pool occurs through the substrate, the previous track and layer as well as the surrounding atmosphere. Although the heat loss through the substrate dominates most of the heat dissipation, other two pathways also play a role. In order to understand the growth of β grains thoroughly, the thermal behavior occurring in AM processes should be carefully analyzed from single tracks to bulk structures.

Fig. 15 shows the cross-section microstructure of an individual track bead built by the authors using the DED technique. The corresponding front view and side view temperature fields in the molten pool and the molten pool geometry predicted by the DED model is presented in Fig. 15(b) and (c) respectively, where the isotherms are indicated by different colors. Apparently, the thermal gradient is perpendicular to the isotherms and heat dissipates from the molten pool downwards into the Ti6Al4V substrate. As a result, the primary β grains nucleate from and then grow perpendicularly to the molten pool/heat affected zone boundary, as validated by the microstructure shown in Fig. 15(a), where the textures of β grains are illustrated by dashed lines. A similar result was also revealed in Wang et al.'s work [139]. When observed from the side view (Fig. 15(c)), the molten pool of the single track is inclined. For a single layer (Fig. 15(d)), the alternate tracks are generated by scanning the laser beam in opposite directions. Taking the rear section of the molten pool, for example, two $\langle 001\rangle_\beta$ directions exist with an opposite inclination angle to the N_z direction (Fig. 15(e)). At the overlapped zone of adjacent tracks, the two directions will be compensated by each other, and the average direction is along the N_z direction. While depositing the second layer, the scan direction is always changed by 45°, and 90° for cubic structures and 60° for cylinders to produce a good geometry. Because the β grain growing in any layer will be tilted away from N_z and the orientation varies in all directions, after depositing several layers the average growth direction will be to N_z but zigzags through layers.

3.2.2. Grain size evolution

The grain size of α′ martensite and α + β lamellae increases with the increase of input energy density. Since AM techniques are layer-by-layer processes, a portion of the previous track and layer will be melted when depositing a following track and layer. The multiple thermal cycles will result in coarsening of grains in the overlapped zones, as

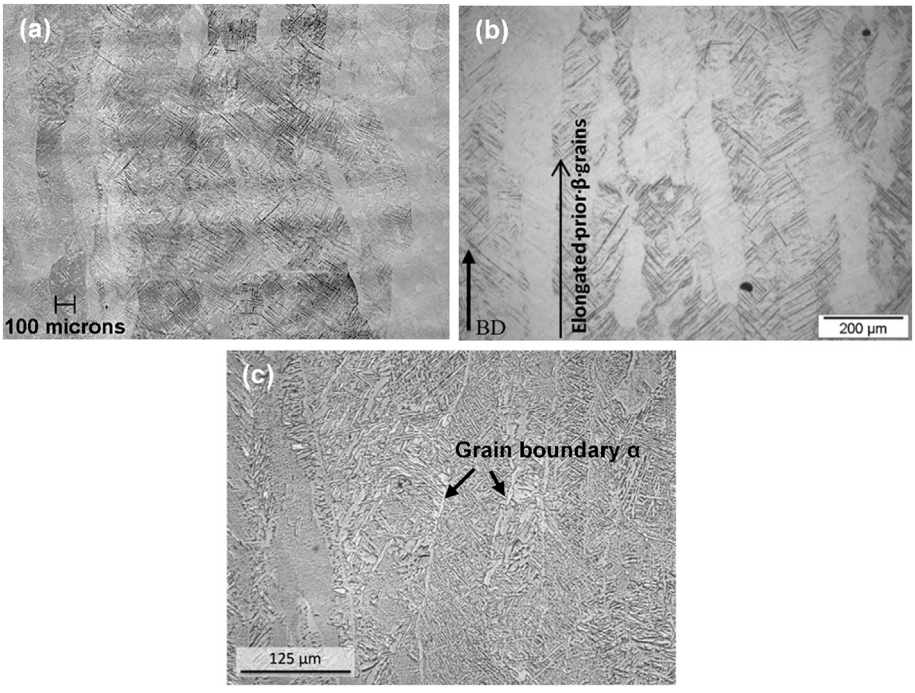

Fig. 14. The morphology of prior β grains formed in (a) directed energy deposited Ti6Al4V. (b) Selective laser melted Ti6Al4V [42]. (c) Electron beam melted Ti6Al4V. Reproduced with permission from Elsevier [99].

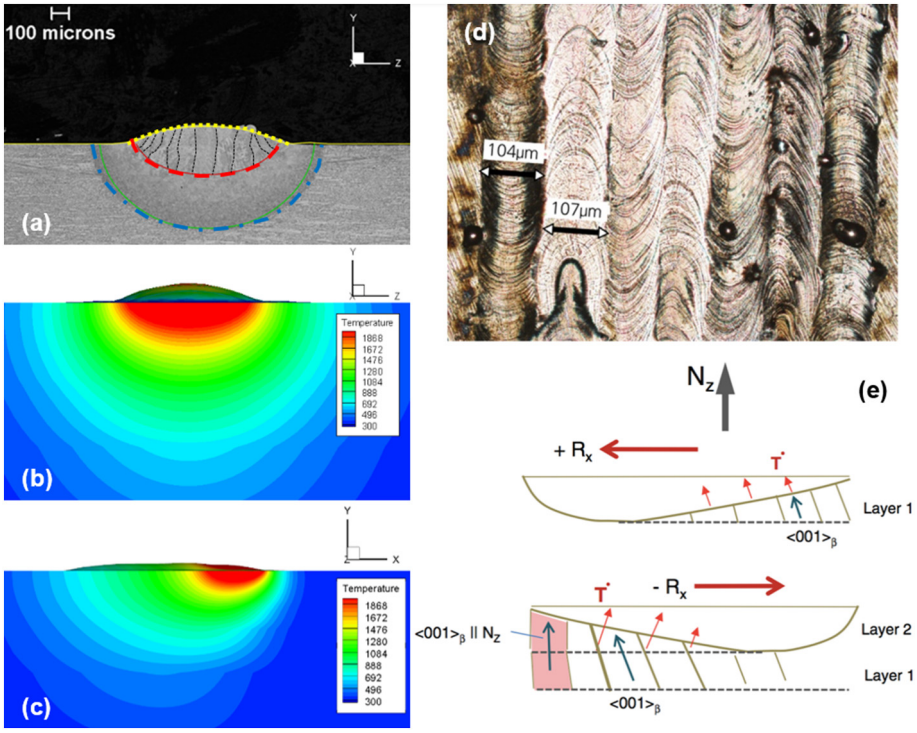

Fig. 15. (a) Single-track bead of directed energy deposited Ti6Al4V illustrates the thermal behavior determining the columnar growth pattern of β grains: (a) Front view of single-track Ti6Al4V microstructure reveals the growth of prior β grains perpendicular to the molten pool boundary (red line). The simulated free surface boundary (yellow line) and heat affected zone boundary (green and blue line) are also imposed. (b) The simulated front view temperature field. (c) The simulated side view temperature field. (d) Single layer Ti6Al4V shows two laser scan directions. Reproduced with permission from Elsevier [16]. (e) Sketch of β grain growth along the thermal gradient [83].

shown by the light-colored layer bands in Fig. 14(a). This phenomenon also applies to different portions of a tall part. Because Ti6Al4V has a very low thermal conductivity of about 7 W/m·K at room temperature [16], the heat will accumulate with increased layer numbers, leading to a higher temperature and a slower cooling rate at the upper zone of Ti6Al4V parts built with SLM and EBM. This situation is a little different from DED manufactured Ti6Al4V where the very top layer still has a high cooling rate due the convection effect induced by argon flow. Qian et al. [74] investigated the microstructure of DED manufactured Ti6Al4V samples and found that the very top and very bottom layers of the samples have a larger amount of martensite than other zones. Carroll et al. [73] conducted the tensile test on the DED manufactured Ti6Al4V specimens extracted from the different zones of the as-built samples. The results show that the specimens extracted from the upper zone along the building direction have lower strength but higher elongation values than those extracted from the lower zone due to the coarsening of microstructures.

As for the EBM process, the sensitivity of α-lath thickness to the built temperature is more distinct. By adjusting the preheating current, the pre-heating temperature of the building chamber can be changed

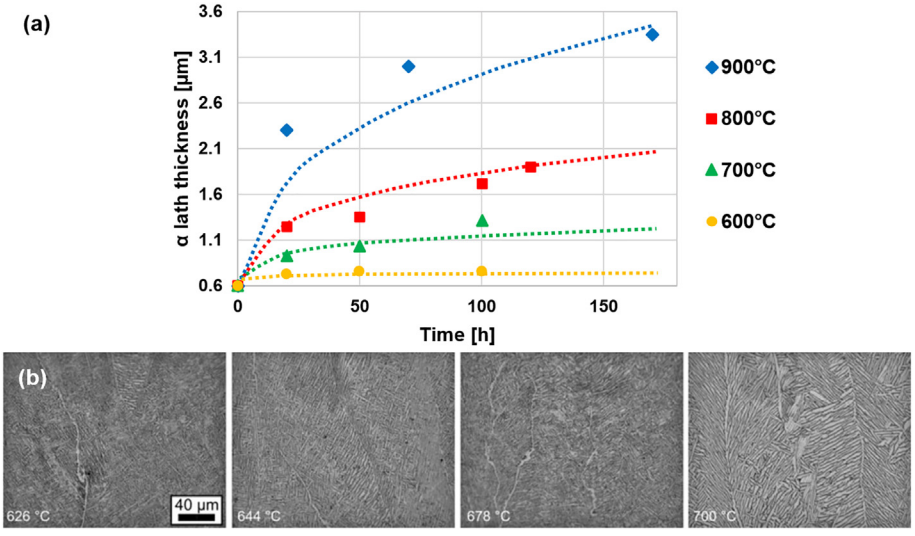

Fig. 16. (a) Experimental (spots) and calculated (dotted lines) values of α-lath thickness as a function of aging time and temperature. Reproduced with permission from Elsevier [31]. (b) The effect of build temperature on the α colony scale. Reproduced with permission from Springer Nature [82].

Table 3
Tensile properties for Ti6Al4V parts built with directed energy deposition (DED), selective laser melting (SLM) and electron beam melting (EBM). The properties of wrought, cast, forged, heat treated and HIPed Ti6Al4V products are included for comparison.

Process	Condition	Specimen orientation	UTS, MPa	YS, MPa	El, %	Ref.
DED	As-built, not machined	Longitudinal	761–821	522–523	–	[49]
	As-built, machined	Longitudinal	984–1050	930–987	–	[49]
	Annealed, not machined	Longitudinal	700–726	621–653	~4.8	[49]
	Annealed, machined	Longitudinal	930–968	812–848	~11.9	[49]
	As-built, not machined	Horizontal	902–923	881–906	~6.4	[49]
	As-built, machined	Horizontal	1033–1109	941–1029	~6.8	[49]
	Annealed, not machined	Horizontal	751–766	620–708	~4.8	[49]
	Annealed, machined	Horizontal	907–967	843–889	~11.9	[49]
	As-built, machined upper tier	Longitudinal	1041 ± 12	945 ± 13	14.5 ± 1.2	[73]
	As-built, machined, lower tier	Longitudinal	1087 ± 8	970 ± 17	13.6 ± 0.5	[73]
	As-built, machined	Longitudinal	1094	1008 ± 2	10.8 ± 0.2	Authors
	As-built, machined	Horizontal	1063 ± 20	960 ± 26	10.9 ± 1.4	[29]
	As-built, machined	Horizontal	1163 ± 22	1105 ± 19	4 ± 1	[146]
	Aged, machined, round sample	Longitudinal	1051–1073	935–947	9.8–13.3	[147]
	Aged, machined, flat sample	Longitudinal	1130–1151	1028–1062	8.4–10.0	[147]
	Aged, machined, round sample	Horizontal	1057–1089	957–989	9.2–10.9	[147]
	Aged, machined, flat sample	Horizontal	1138–1168	1014–1085	3.4–8.4	[147]
	As-built, machined, low power	Horizontal	1103	1005	4	[72]
	As-built, machined, high power	Horizontal	1042	990	7	[72]
	Aged, machined, low power	Horizontal	1073	1000	9	[72]
	Aged, machined, high power	Horizontal	1044	991	10	[72]
	Stress-relieved, machined	–	956	907	10.8	[144]
	Stress-relieved, HIPed, machined	–	900	829	15.4	[144]
SLM	As-built, machined	Horizontal	1211 ± 31	1100 ± 12	6.5 ± 0.6	[84]
	Annealed, machined	Horizontal	1042 ± 20	960 ± 19	13.0 ± 0.6	[84]
	As-built, machined	Horizontal	1095 ± 10	990 ± 5	8.1 ± 0.3	[148]
	As-built, machined	Longitudinal	1246 ± 134	1150 ± 67	1.4 ± 0.5	[58]
	As-built, machined	Horizontal	1421 ± 120	1273 ± 53	3.2 ± 0.5	[58]
	As-built, machined	Longitudinal	1166 ± 25	962 ± 47	1.7 ± 0.3	[87]
	Annealed (high temperature, supersolvus), machined	Longitudinal	951 ± 55	836 ± 64	7.9 ± 2	[87]
	Annealed (high temperature, substransus), machined	Longitudinal	1040 ± 4	925 ± 14	7.5 ± 2	[87]
	Annealed (low temperature), machined	Longitudinal	1000 ± 53	900 ± 101	1.9 ± 0.8	[87]
	As-built, machined	Horizontal	1206 ± 8	1137 ± 20	7.6 ± 2	[87]
	Annealed (high temperature, supersolvus), machined	Horizontal	1019 ± 11	913 ± 7	8.9 ± 1	[87]
	Annealed (high temperature, substransus), machined	Horizontal	1036 ± 30	944 ± 8	8.5 ± 1	[87]
	Annealed (low temperature), machined	Horizontal	1046 ± 6	965 ± 16	9.5 ± 1	[87]
	As-built, machined	Horizontal	1267 ± 5	1110 ± 9	7.28 ± 1.12	[51]
	As-built, machined	Longitudinal	1219 ± 20	1143 ± 30	4.89 ± 0.6	[103]
	As-built, machined	Horizontal	1269 ± 9	1195 ± 19	5 ± 0.5	[103]
	As-built, not machined	Longitudinal	1040–1062	664–802	11.3–12.7	[48]
	As-built, machined	Longitudinal	1151–1157	984–988	10.2–11.3	[48]
	Annealed (700 °C), machined	Longitudinal	1115–1116	1045–1054	9.5–12.4	[48]
	Annealed (900 °C), machined	Longitudinal	987–989	905–911	7.4–12.5	[48]
	HIPed, machined	Longitudinal	973–974	883–888	18.5–19.4	[48]
	As-built, machined	Longitudinal	1117 ± 3	967 ± 10	8.9 ± 0.4	[141]
	Stress-relieved, machined	Longitudinal	1052 ± 11	937 ± 9	9.6 ± 0.9	[141]
	As-built, machined	Horizontal	1137–1248	973–1100	7.1–12.3	[141]
	Stress-relieved, machined	Horizontal	1049–1086	952–981	6.5–13.1	[141]
	As-built, not machined	Horizontal	1035 ± 29	910 ± 9.9	3.3 ± 0.76	[108]
	As-built, machined	–	1080 ± 30	1008 ± 30	1.6 ± 2	[47]
	Annealed (800 °C), machined	–	1040 ± 30	962 ± 30	5 ± 2	[47]
	Annealed (1000 °C), machined	–	945 ± 30	798 ± 30	11.6 ± 2	[47]
	HIPed, machined	–	1005 ± 30	912 ± 30	8.3 ± 2	[47]
	Stress relieved, machined	Longitudinal	1032	961	2.7	[71]
	Stress relieved, machined	Longitudinal	1140	1070	–	[101]
	As-built, not machined	–	960 ± 2	850 ± 6	6.8 ± 0.5	[132]
EBM	As-built, not machined	Longitudinal	851 ± 19	812 ± 12	3.6 ± 0.9	[149]
	As-built, not machined	Horizontal	833 ± 22	783 ± 15	2.7 ± 0.4	[149]
	As-built, machined, interior location	Longitudinal	1032.9 ± 12.9	984.1 ± 8.5	9.0 ± 2.9	[133]
	As-built, machined, exterior location	Longitudinal	1008.6 ± 15.2	961 ± 7.1	7.1 ± 3.4	[133]
	As-built, machined, interior location	Horizontal	1029.7 ± 7	982.9 ± 5.7	12.2 ± 0.8	[133]
	As-built, machined, exterior location	Horizontal	1017.4 ± 4.9	966.5 ± 5.3	12.2 ± 2.0	[133]
	As-built, machined	Longitudinal	972 ± 14	845 ± 9	14.2 ± 1.5	[58]
	As-built, machined	Horizontal	976 ± 11	846 ± 7	15.0 ± 2.0	[58]
	As-built, machined	Longitudinal	1045	970	10.9	[71]
	As-built, machined	Longitudinal	1073–1116	1001–1051	11–15	[72]
	As-built, machined	Horizontal	1032–1066	973–1006	12–15	[72]
	As-built, machined	Longitudinal	928 ± 9.8	869 ± 7.2	9.9 ± 1.7	[103]
	As-built, machined	Horizontal	978 ± 3.2	899 ± 4.7	9.5 ± 1.2	[103]
	As-built, not machined	–	790 ± 10	740 ± 10	2.2 ± 0.3	[132]
	Annealed, machined	–	837–918	741–842	3–9	[50]
	HIPed, machined	–	817–918	723–817	3–9	[50]
	Stress relieved, machined	–	885–1015	778–943	3–9	[50]
Wrought	–	Longitudinal	942 ± 8	836 ± 9	12.5 ± 1.2	[58]

Table 3 (*continued*)

Process	Condition	Specimen orientation	UTS, MPa	YS, MPa	El, %	Ref.
	–	Horizontal	933 ± 7	832 ± 10	13.0 ± 1.5	[58]
	–	–	1063	966	~13.8	[49]
	–	–	870 ± 10	790 ± 20	18.1 ± 0.8	[148]
	–	–	995	930	14	[87]
	–	–	960 ± 10	880 ± 3	14 ± 4.1	[132]
Forged	Mill annealed	–	1030	970	16	[72]
	Mill annealed	–	1006 ± 10	960 ± 10	18.37 ± 0.88	[51]
Cast	–	–	980	865	13.5	[87]
	–	–	875 ± 10	750 ± 2	4.5 ± 0.2	[132]
ASTM F136	–	–	>860	>795	>10	[58,84]

Note: UTS, YS, El, HIP represent ultimate tensile strength, yield strength, elongation, hot isostatic pressing, respectively.

from 600 °C to 750 °C [70–72]. The effect of build temperature on the α colony scale is shown in Fig. 16(b) [82]. With the increased preheating temperature, the α-lath thickness increases obviously. The coarsening effect is in an agreement with the annealing conducted at different temperatures (Fig. 16(a)). At 600 °C, coarsening of α-lath is not significant and is almost independent of holding time, while higher temperatures of 700–800 °C dramatically increase the thickness of α-lath and the coarsening effect increases with the increase of holding time.

4. Properties of AM manufactured Ti6Al4V products

A crucial consideration in any AM technique is if competitive or improved material properties can be achieved as compared to the components fabricated by traditional manufacturing methods. Mechanical properties, particularly tensile and fatigue properties, are the mostly used properties to evaluate the performance of load-bearing Ti6Al4V materials. In this section, the tensile and fatigue properties of as-built AM Ti6Al4V products are discussed.

4.1. Tensile test properties

The uniaxial standard tensile tests are usually conducted on cylindrical bars or dog-bone shaped specimens, which are directly built to net shapes or machined from as-built samples and tested according to ASTM E8. Ti6Al4V alloy possesses remarkable strain-rate and temperature sensitivity. Li et al. [88] conducted the tensile test on the DED manufactured Ti6Al4V parts at both low and high strain rates with increased temperatures. At low stain rates, the tensile fractures exhibited composite fracturing morphologies including both quasi-cleavages and dimples, while only ductile dimples were observed for high-strain-rate fractures. With the test temperature increasing from room temperature to 1173 K, the strength dropped by about 60%. The reason associated with this phenomenon is that the increased temperature reduces the dislocation density, and hence loses the resistance to plastic flow. In order to make a consistent comparison for the mechanical performance, this review only focuses on the low-strain-rate mechanical tests conducted at room temperature. Table 3 provides a summary of the tensile test properties obtained on Ti6Al4V parts manufactured by DED, SLM and EBM, as compared with those produced by traditional manufacturing methods and post-processing conditions. It should be noted that, in this paper, the longitudinal and horizontal orientations indicate samples extracted in parallel and perpendicular directions to the building direction (Z axis), respectively (Fig. 17).

4.1.1. Effects of phase and grain size on tensile properties

As shown in Table 3, a considerable increase in UTS and YS is observed for the DED and SLM samples compared to EBM, wrought and heat treated samples. However, laser-based AM parts only have an elongation in the range of 4–11%, which is substantially lower than the 10–17% elongation produced by EBM and wrought processes. It needs to be noted that all these properties are compared for the specimens with a machined finish since the as-built surfaces of AM samples dramatically degrade the properties. Various heat treatment processes function differently in altering the properties of as-built parts. Pure stress-relieved heat treatment is generally conducted at temperatures below 800 °C, which will hardly coarsen the microstructure and hence only increase the ductility by about 1–2%. The high temperature annealing above 800 °C, on the contrary, will definitely coarsen the microstructure, leading to a remarkably improved elongation but at a sacrifice of strength. The HIP has been explained previously that it can help close the pores and densify the microstructure, which is favorable in increasing the ductility. Aging is known not to dramatically decrease the strength although high temperature is involved because the precipitation of Ti_3Al during aging may result in precipitation strengthening [150].

The mechanical properties of Ti6Al4V depend largely on its microstructure, including constituent phases, size scales of grains, the texture of prior β grains as well as the presence of defects. Among these factors, the crystal structure that changes from one phase to another plays a major role in defining Ti6Al4V properties. Galarraga et al. [31] studied the values of UTS, YS, and El for different types of Ti6Al4V microstructures. The results were illustrated in Fig. 18, which shows that α′ martensite has the highest strength value among all the microstructures. The strength of columnar α + β microstructure is higher than that of equiaxed α + β. However, the strength and ductility exhibit contrasting trends. The fine needle-shaped α′ martensite has a serious reduction of plasticity. Galarraga et al. [31] also reported a similar evolution of hardness to that of UTS for different microstructures.

As laser-based AM Ti6Al4V components consist of complete acicular α′ martensite while EBM parts have an α + β microstructure, it is

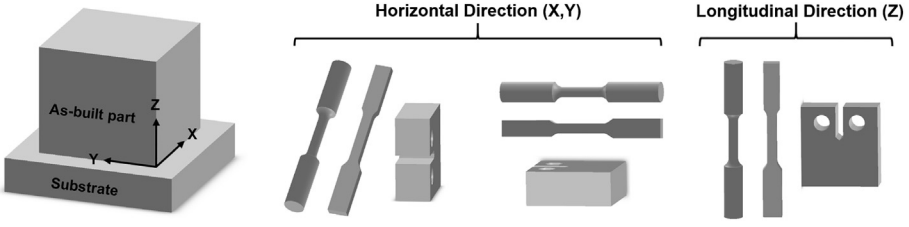

Fig. 17. Illustration of the deposit geometry and the extracted orientations of tensile test specimens. Both X and Y directions are belonged to the horizontal direction while Z direction is longitudinal direction.

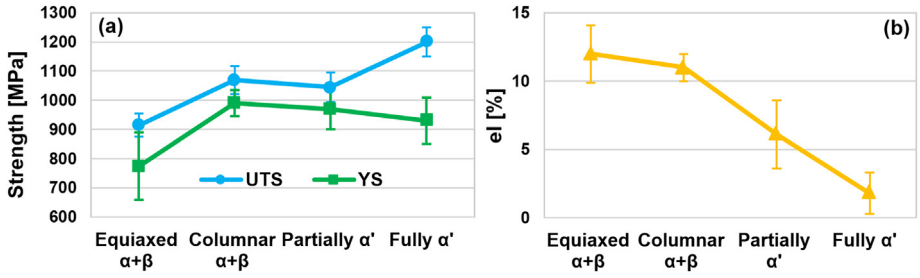

Fig. 18. (a) Ultimate strength (UTS), yield strength (YS) and (b) elongation (el) values for different Ti6Al4V microstructures related to different cooling rates. Equiaxed α + β, columnar α + β, partially α′ and fully α′ correspond to furnace-cooling, EBM-built, air-cooling, and water-cooling condition, respectively. Reproduced with permission from Elsevier [31].

reasonable that DED and SLM samples exhibit a higher strength but lower ductility than those built by EBM. The underlying strengthening mechanisms associated with different microstructures result from phases and hardening mechanisms. Martensitic α′ is a non-equilibrium phase with deformed lattice structures. Its formation will incur lattice strains, and hence it is stronger than α + β phases. In addition, a high density of dislocations is observed in α′ martensites [124], which results in hardening via dislocation strengthening [136,151].

Different from laser-based AM processes, the high build temperature in EBM process will decompose α′ martensite into α + β, and also eliminate the thermal stresses. Under such circumstances, the final strength of EBM parts is strongly dependent on the thickness of α-lath in the balanced α + β lamellar microstructure [152]. Fig. 19 illustrates the relationship between tensile properties and the thickness of α-lath [31]. With the increase of α-lath thickness, the yield strength decreases because the thicker α-lath increases the effective slip length and hence reduces the yield strength. A slight increase in elongation is observed when the thickness of α-lath increases from 0.5 μm to 1 μm and then the elongation continuously decreases as the α-lath thickness increases. It should be noted that the ultimate strength is almost free from the influence of α-lath thickness.

4.1.2. Oxygen contamination

In some cases of AM parts built with even optimized deposition parameters, the ductility of as-built parts remains low despite the absence of porosity. One possible reason is contaminations (e.g., oxygen, nitrogen and/or hydrogen) in shielding gases [99,153]. Ti and its alloys have a very high affinity to oxygen, nitrogen and hydrogen, and an increased temperature will facilitate the reaction between these gases and Ti [82]. Donachie [1] found that the fabrication of Ti products must be under atmospheric protection to prevent oxygen contamination when temperature exceeds 700 K. Since the building chamber for EBM is only pumped out to about 10^{-4}–10^{-5} mbar and that for the DED and SLM can only maintain a 5–10 ppm atmosphere, some oxygen, nitrogen and water molecules would be still present. de Formanoir et al. [99] pointed out that the oxygen content in EBM parts is above 0.23%. An excessive amount of oxygen was also detected in the recycled powder. Contamination of oxygen can be judged by the surface color of AM Ti6Al4V parts. With the increase in contamination degree, the part's surface color changes from silver to straw and further to blue [153], which indicates an increased oxide film thickness with increased surface hardness [73].

In addition to the influence on hardness, oxygen and nitrogen are also known as alpha phase stabilizer and will strengthen and stabilize the alpha phase. In deformation, they will pin the dislocation and affect the material's tensile behavior [154]. This effect is demonstrated by a slight increase in ultimate and yield strength but a decrease in ductility. For example, Carroll et al. [73] reported that an extra 0.0124 wt% O results in an improved ultimate and yield strength by 9 MPa and 16 MPa, respectively. However, the introduction of oxygen will weaken the plastic deformation by replacing the ductile dimple structure with relatively brittle quasi-cleavage morphology [153]. When the oxygen content amounts to 10% or higher, the weld specimen showed little signs of plastic deformation and the fracture mode changed completely from ductile to brittle [153]. In order to avoid oxygen contamination, protection must be provided during the use of powders, and recycling of powders should be limited, considering that the oxygen content in powders increases during handling and recycling [99].

4.1.3. Anisotropy

It is shown in Table 3 that AM built Ti6Al4V components show a significant anisotropy in tensile properties in different orientations. The longitudinal specimens generally have 20–30 MPa lower UTS and YS than horizontal samples but elongation increases by about 2%. The macro-mechanical properties in longitudinal and horizontal directions are associated with the anisotropic microstructure: the elongated columnar β grains and the presence of grain boundary α. As shown in Fig. 14, β grains grow longitudinally along the deposition direction with a length of about 20 mm while the width of the prior β grains is only about several hundred microns. Along the long axis of β grain, a thin layer of grain boundary α will be formed, delineating the β grains (Fig. 14(c)). The presence of these grain boundary α phases destroys the microstructure integrity and behaves like a weak band connector. Simonelli et al. [141] pointed out that the grain boundary α tends to serve as a path along the prior β grain boundaries, along which damage can preferentially accumulate.

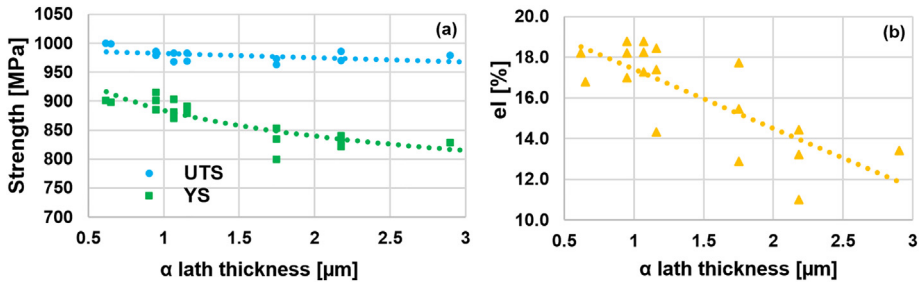

Fig. 19. (a) Ultimate strength (UTS) and yield strength (YS) and (b) elongation (el) values versus α-lath thickness and empirical correlations. The standard deviations are as 50 MPa for the UTS and 72 MPa for the YS and 2.5% for el. Reproduced with permission from Elsevier [31].

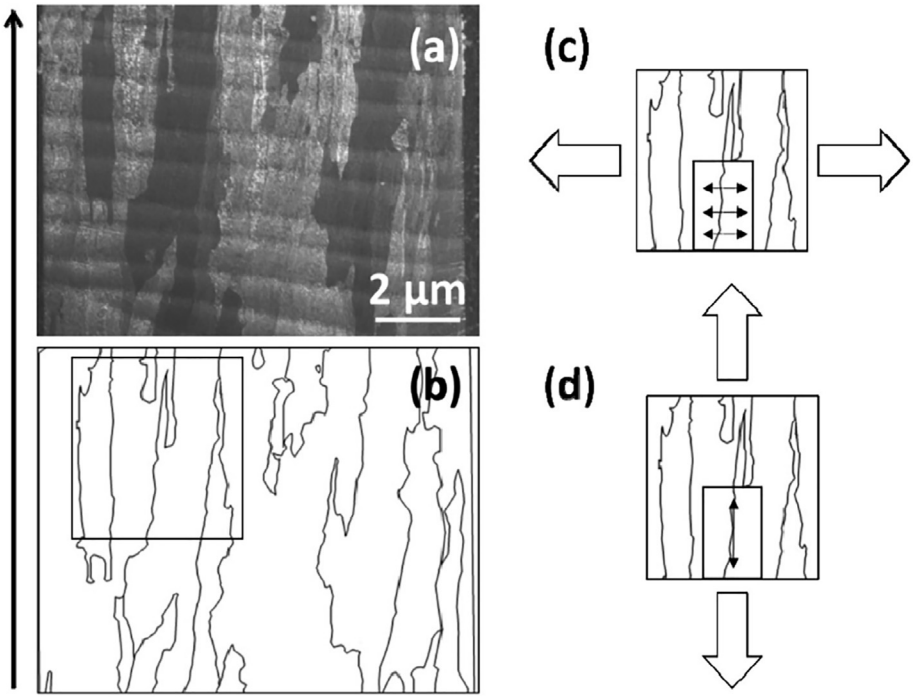

Fig. 20. Schematic plot illustrates the anisotropy behavior of AM produced Ti6Al4V components that are subjected to the tension loads applied along (a) horizontal and (b) longitudinal directions. Reproduced with permission from Elsevier [73].

Fig. 20 illustrates the anisotropy behavior of AM produced Ti6Al4V components that are subjected to the tension loads applied along the horizontal (Fig. 20(a)) and longitudinal (Fig. 20(b)) directions [73]. When exposed to the tension in the horizontal direction, the tensile loads are exerted on the short axes of β grains and grain boundary α acting to separate adjacent β grains. On the contrary, the long axes of β grains and the entire grain boundary α are subjected to the longitudinal tensile loads. Therefore, the anisotropic microstructure predisposes the horizontal specimens much more easily to failure compared to the longitudinal specimens. Consequently, the longitudinal samples tend to have a higher elongation value. However, if lack-of-fusion pores prevail in the samples, the situation will be opposite.

4.2. Fatigue properties

Fatigue failure, due to the damage caused by cyclic stresses, is one of the most common failure modes. For example, Ti6Al4V compressors and turbine blades in aircraft or automobile engines are subject to high frequency cyclic loadings with frequencies larger than 1 kHz [155]. Estimation of fatigue performances usually is done by adopting stress-life (*S-N*) or strain-life (ε-*N*) approaches, where *N* indicates the cycles to failure. The stress intensity factor before crack propagates (crack propagation threshold, ΔK_{th}) and fatigue limit before crack propagates (threshold stress, $\Delta\sigma_w$) [44] are two typical parameters characterizing the microscopic crack initiation while the cycles to failure are generally macroscopic characteristics for fatigue performance. It needs to be pointed out that the stress ratio (ratio of minimum stress to maximum stress in one cycle of loading in a fatigue test, *R*) affects the fatigue limit (Table 4). In order to avoid the discrepancy caused by various *R* conditions, Li et al. [69] uses σ_{eff} in terms of the actual maximum value of the applied stress (σ_{max}) at an given *R* to normalize different *R* values, which is represented by:

$$\sigma_{eff} = \sigma_{max}\left(\frac{1-R}{2}\right)^{0.28} \quad (6)$$

Till now many studies have been carried out on fatigue performances of AM manufactured Ti6Al4V products. Table 4 summarizes the fatigue properties of DED, SLM and EBM built Ti6Al4V in the as-built condition as compared to those of conventionally fabricated and post-treated Ti6Al4V products. The surface machining is necessary for as-built samples since the surface defects will deteriorate the fatigue performance. Compared with EBM, the as-built Ti6Al4V parts fabricated by DED and SLM have a higher $\Delta\sigma_w$ but lower ΔK_{th}, which indicates that laser-based AM processes produce higher fatigue strength but lower fatigue toughness than EBM. After annealing and stress-relieving heat treatments, the ΔK_{th} value for DED and SLM built Ti6Al4V parts increases with the increased temperature, and is comparable to the as-built parts fabricated by EBM. Compared with other post-processing methods, HIP dramatically improves both the fatigue strength and fatigue toughness since HIP can effectively reduce the pores, which are known serving as the crack initiation points. Comparisons between the tests conducted in horizontal and vertical directions reveal a slight difference in $\Delta\sigma_w$ and ΔK_{th} values. This indicates that the anisotropic structure in AM Ti6Al4V also affects the fatigue properties.

The major factors causing the fatigue failure revealed in literature are applicable to products built by every manufacturing method: These factors are surface quality, residual stresses, pores and microstructure [69] (see Fig. 21). In Fig. 21(d), smooth facets are also found to be responsible for the initiation of crack failure [162], but these facets more prevail in wrought specimens which are free from porosity [135]. It should be mentioned that although the fatigue data presented in this review are for AM Ti6Al6V, many of the influences are applicable to other alloys and different manufacturing methods [44].

4.2.1. Influences of microstructure on fatigue properties

Compared to EBM Ti6Al4V, the as-built DED and SLM Ti6Al4V parts have higher fatigue strength ($\Delta\sigma_w$) but lower fatigue toughness (ΔK_{th}). The superior fatigue strength of DED and SLM built Ti6Al4V should result from the presence of fine α′ martensite [72,103], which contains a high density of dislocations. Along with the further impeding of dislocation motion caused by the fine structure, the dislocation strengthening effect will be enhanced at a sacrifice of plastic strain.

Table 4
The fatigue properties of DED, SLM and EBM built Ti6Al4V in the as-built condition as compared to those of conventionally fabricated and post-treated Ti6Al4V products.

Process	Condition	Specimen orientation	R	$\Delta\sigma_w$, MPa	ΔK_{th}, MPa $\sqrt{m}$	Ref.
DED	As-built, machined, low power	Longitudinal	0.1	–	2.8	[72]
	As-built, machined, high power	Longitudinal	0.1	–	3.5	[72]
	Aged, machined, low power	Longitudinal	0.1	–	3.0	[72]
	Aged, machined, high power	Longitudinal	0.1	–	3.8	[72]
	As-built, machined, low power	Horizontal	0.1	–	2.8	[72]
	As-built, machined, high power	Horizontal	0.1	–	3.4	[72]
	Aged, machined, low power	Horizontal	0.1	–	2.9	[72]
	Aged, machined, high power	Horizontal	0.1	–	3.2	[72]
	As-built, machined	Longitudinal	0.1	587.5–600	–	[156]
	As-built, machined	–	−1	~500	–	[157]
SLM	As-built, machined	Longitudinal	0.1	–	1.7	[47]
	Annealed (800 °C), machined	Longitudinal	0.1	–	3.7	[47]
	Annealed (1050 °C), machined	Longitudinal	0.1	–	6.1	[47]
	HIPed, machined	Longitudinal	0.1	620 ± 5.4	4	[47]
	As-built, machined	Horizontal	0.1	–	1.4	[47]
	Annealed (800 °C), machined	Horizontal	0.1	–	3.9 ± 0.4	[47]
	Annealed (1050 °C), machined	Horizontal	0.1	–	3.9 ± 0.4	[47]
	HIPed, machined	Horizontal	0.1	620 ± 5.4	3.9 ± 0.4	[47]
	Stress relieved, not machined	Longitudinal	0.1	210	–	[101]
	Stress relieved, machined	Longitudinal	0.1	500	3.48	[101]
	As-built, machined	–	0.1	550	–	[103]
	HIPed, not machined	–	−1	200	–	[48]
	HIPed, machined		−1	350	–	[48]
EBM	As-built, machined	Longitudinal	0.3	–	4.0–4.8	[158]
	HIPed, machined	Longitudinal	0.3	–	4.7–5.1	[158]
	As-built, machined	Horizontal	0.3	–	3.4–5.0	[158]
	As-built, machined	Horizontal	0.1	–	3.8	[158]
	HIPed, machined	Horizontal	0.3	–	4.8–5.0	[158]
	As-built, machined	–	0.1	340	–	[103]
	As-built, machined	–	0.1	200–250	–	[45]
	Stress relieved, machined	–	0.1	200–250	–	[45]
	HIPed, machined	–	0.1	550–600	–	[45]
Wrought		–	−1	600	–	[48]
		–	−1	630–680	–	[159]
Forged		–	−1	425	13	[160]
	Mill annealed	–	−1	590–605	9	[160]
	Solution treated	–	−1	590	10	[160]
		–	0	–	7	[160]
	Mill annealed	–	0	–	4.4–4.7	[160]
	Solution treated	–	0	–	4.9–5.2	[160]
		–	0.7	–	3	[160]
	Mill annealed	–	0.7	–	2.4	[160]
	Solution treated	–	0.7	–	2.4	[160]
	Mill annealed	–	0.1	–	4.4	[72]
Cast	As built	–	0.1	150–270	–	[161]
	Machined	–	0.1	230–380	–	[161]
	Annealed	–	0.1	430	–	[103]

[103]. After annealing of the initial SLM microstructure, an increase in ΔK_{th} to the same level of EBM built parts is observed due to the decomposition of α′ martensite [72] and the removal of residual stresses. As for the α + β microstructure, similarly to tensile strength, fatigue performance will be improved when the size of α phase decreases [164–166]. A qualitative study conducted by Lütjering et al. [165] revealed a 20% increase in fatigue strength (approximately 500–600 MPa) when the thickness of α-lath decreases from 10 μm to 1 μm.

In terms of specimens that are free from defects for crack initiation, plastic slip localization will become the new candidate for crack initiation. Generally, a fine microstructure is known to have a higher fatigue strength. One reason is because the grain and phase boundaries will impede the localization of plastic slip. In Ti6Al4V with an α + β microstructure, the localization of plastic slip prevails in the hcp α phase (Fig. 21(c)). Polasik [166] confirmed this phenomenon by showing that crack nucleation starts from α phase in both equiaxed and lamellar shape in the absence of defects. Zhai et al. [72] further proved that crack interaction with fine α colonies is the leading reason for the development of crack. As the crack tip driving force (ΔK) increases, crack propagates and begins to interact with β. As the thickness of α phase decreases, the resistance to long plastic slip bands increases, leading to a higher resistance to fatigue crack initiation [167].

4.2.2. Defects

As explained in Section 2.3, the AM parts are plagued by the surface roughness and internal porosity in the as-built state. These defects have a significant impact on the fatigue performance because they will become the fatigue crack initiation sites (Fig. 21(a, b, d, e)). Günther et al. [163] discovered that the failure mechanisms are driven quite differently by surface and internal defects (Fig. 22), in consistency with the case of traditionally manufactured Ti6Al4V as shown by Heinz et al. [168]. As clearly shown in Fig. 22, the surface finish quality is much more detrimental as compared to internal defects. Shorter fatigue lives are associated with the surface defects, while the internal defects require a higher number of cycles to failure [71]. It has been confirmed that the surface roughness acts as multiple stress concentrators, and behaves like short cracks [169]. For AM Ti6Al4V, the as-built parts without surface machining only exhibit a fatigue performance about 40–50% of that after machining [101,159,170,171]. One responsible reason associated with this phenomenon can be attributed to the increased stress concentration induced by the pores at or near the surface [172]. It is

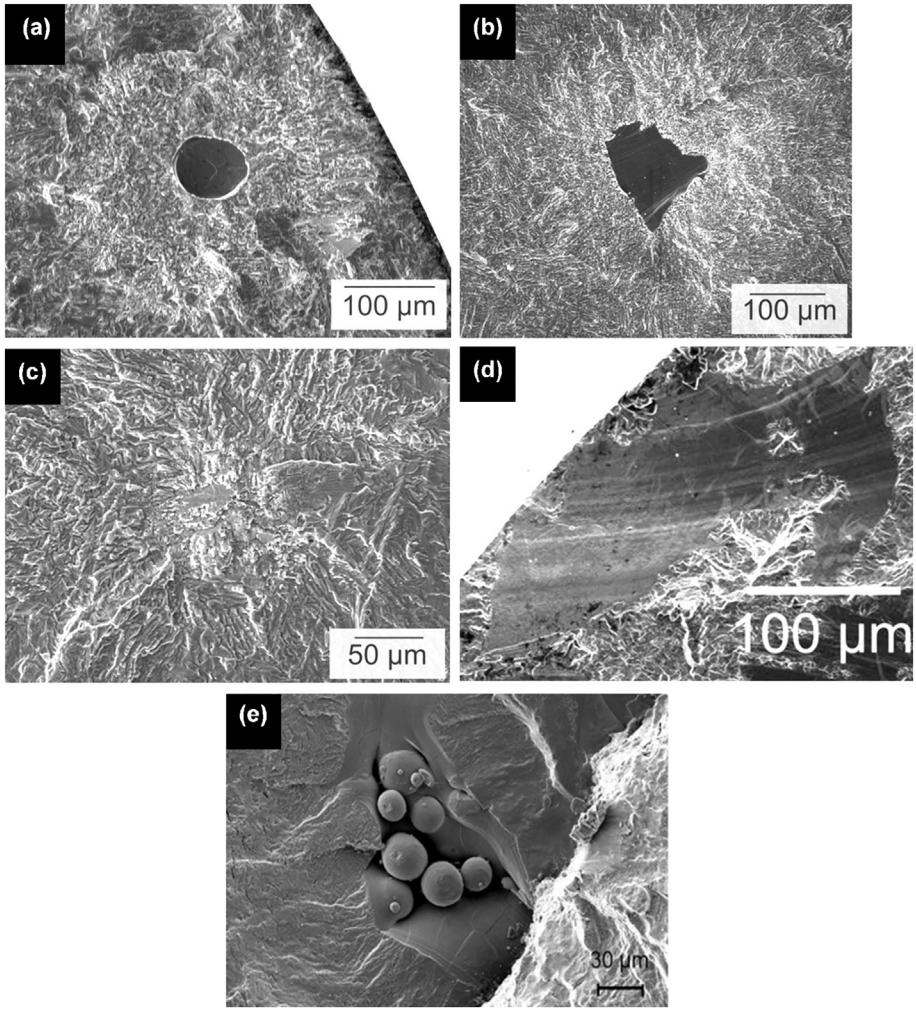

Fig. 21. Fatigue crack initiation from defects in Ti6Al4V specimens: (a) An inner gas pore. Reproduced with permission from Elsevier [163]. (b) Lack-of-fusion. Reproduced with permission from Elsevier [163]. (c) α phase. Reproduced with permission from Elsevier [163]. (d) A smooth facet. [162]. (e) Unmelted Ti6Al4V powder particles at the external surface. Reproduced with permission from Elsevier [48].

noteworthy that Tammas-Williams et al. [162] found a crack initiating from a large interior pore appears to nucleate not at the greatest tensile stress concentration but at a higher shear stress zone nearby, indicating the dominant role of shear within persistent slip bands in affecting the initiation of fatigue cracks and the early growth of these cracks.

In addition to the distribution, the size and shape of defects also affect the fatigue properties to a great extent. The cross sectional area of a defect normal to the applied stress (A_n) has a larger effect on the fatigue life than its volume [173]. In general, the fatigue failure occurs first at the largest defect if the shape factor is similar for all defects (Fig. 23(a)). However, the shape of the defects also plays a key role in fatigue crack initiation (Fig. 23(b)) [162]. In Fig. 23(b), with an increased aspect ratio of the pore, the stress concentration (K_t) increases, indicating a larger probability in crack initiation. The similar effect can

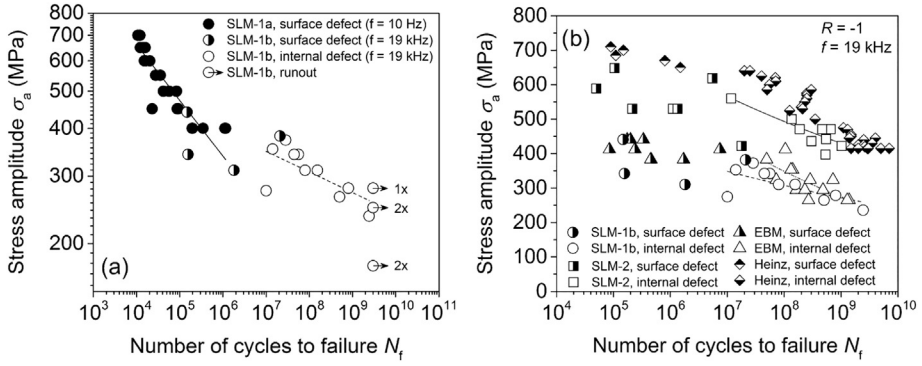

Fig. 22. Stress-number of cycles to failure (S-N) curves of selective laser melting (SLM) built Ti6Al4V samples subjected to two different heat treatment conditions (SLM-1a and SLM-1b): (a) Fatigue tests for SLM-1a and SLM-1b subjected to conventional (10 Hz) and ultrasonic (19 kHz) frequency loads, (b) S-N curves of SLM-1b, SLM-2, EBM and conventionally processed material recompiled from Heinz et al. [168] determined by ultrasonic fatigue testing. Reproduced with permission from Elsevier [163].

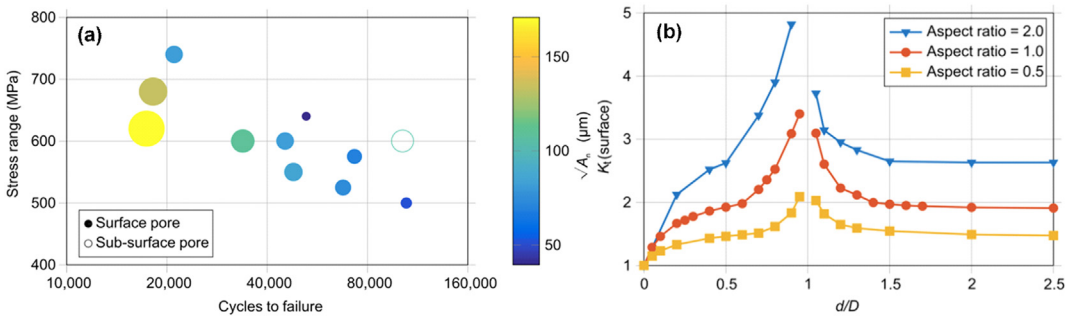

Fig. 23. (a) Effect of pore size on fatigue life and (b) the stress concentration (K_t) generated by idealized spheres/oblate spheroids with different aspect ratios vs dimensionless pore location calculated by dividing the maximum depth from the surface (d) by the pore diameter (D) [162].

also be confirmed by the gas pore and lack-of-fusion pore (Section 2.3.1). The lack-of-fusion pores definitely have an aspect ratio larger than 1.0 while the gas pore can be considered to have an aspect ratio close to 1.0 due to its round shape. The sharp tips of the long axis of lack-of-fusion pores are known to incur higher and more concentrated stresses, which will initiate cracks more easily.

4.2.3. Residual stresses

The presence of residual stresses in a metallic structure is a direct reason causing the crack initiation. It should be noted that residual stresses consist of tensile and compressive stresses. Residual stresses in compression are beneficial to the fatigue properties while tensile residual stresses function deleteriously [174], because they can provide additional driving force for crack initiation and propagation [175]. Due to the high thermal gradients, laser-based AM processes are prone to a larger amount of residual stresses where the tensile stresses are distributed at the surface and near surface zone [108], as explained in Section 2.3.3. Different from DED and SLM, EBM specimens are almost free from residual stresses because of the high build temperature. For example, Hrabe et al. [45] studied fatigue behaviors of EBM fabricated Ti6Al4V parts in as-built and stress-relieved conditions, and obtained a similar fatigue strength in both conditions, which further confirms the negligible residual stresses in the EBM process.

5. Conclusions

In this paper, microstructures and tensile and fatigue properties of DED, SLM and EBM built Ti6Al4V components were comparatively studied with the consideration of fabrication limitations, and the results were compared with the counterparts built with other methods. A summary of the findings is provided below:

1. DED and SLM processes produce peak temperatures about 2000–2500 K and high cooling rates about 10^4 K/s in fabrication of Ti6Al4V. EBM generates a similar peak temperature range but the high build temperature of 600–750 °C decreases the cooling rate locally.
2. The thermal behaviors of DED and SLM processes result in an acicular α′ martensitic microstructure and high tensile stresses while the high build temperature involved in the EBM process leads to an α + β lamellar microstructure free from residual stresses.
3. The presence of α′ martensite in DED and SLM Ti6Al4V significantly increases the ultimate tensile and yield strength by 100–200 MPa but decreases the ductility of the as-built components as compared to the EBM parts that present a similar strength value and moderate ductility to traditionally manufactured and post-treated Ti6Al4V components.
4. α′ martensites in DED and SLM Ti6Al4V are also responsible for the lower crack thresholds but higher fatigue limits as compared to EBM, wrought, forged and heat treated Ti6Al4V.
5. The surface roughness, porosity and high tensile stresses in AM Ti6Al4V serve as crack initiation. The location and shape of defects also play a vital role in determining the fatigue performances.
6. Post machining and heat treatments can significantly weaken the crack initiation and increase the fatigue life of AM fabricated Ti6Al4V.

CRediT authorship contribution statement

Shunyu Liu: Conceptualization, Writing - original draft. **Yung C. Shin:** Supervision, Writing - review & editing.

CRediT authorship contribution statement

Shunyu Liu: Conceptualization, Writing - original draft. **Yung C. Shin:** Supervision, Writing - review & editing.

Acknowledgement

During the course of this study, SL was supported by the Donald A. & Nancy G. Roach Professorship at Purdue University and Purdue EFC Future Manufacturing Seed Grant.

References

[1] M.J. Donachie, Titanium: A Technical Guide, second ed. ASM International, Materials Park, OH, 2000.
[2] C. Cui, B. Hu, L. Zhao, S. Liu, Titanium alloy production technology, market prospects and industry development, Mater. Des. 32 (3) (2011) 1684–1691.
[3] I. Inagaki, T. Takechi, Y. Shirai, N. Ariyasu, Application and features of titanium for the aerospace industry, Nippon Steel & Sumitomo Metal Technical Report 2014, pp. 22–27.
[4] R.R. Boyer, An overview on the use of titanium in the aerospace industry, Mater. Sci. Eng. A 213 (1) (1996) 103–114.
[5] P. Singh, H. Pungotra, N.S. Kalsi, On the characteristics of titanium alloys for the aircraft applications, Mater. Today Proc. 4 (8) (2017) 8971–8982.
[6] E. Uhlmann, R. Kersting, T.B. Klein, M.F. Cruz, A.V. Borille, Additive manufacturing of titanium alloy for aircraft components, Proc. CIRP 35 (2015) 55–60.
[7] N.A. Waterman, P. Dickens, Rapid product development in the USA, Europe and Japan, World Class Des. Manuf. 1 (3) (1994) 27–36.
[8] C. Emmelmann, P. Scheinemann, M. Munsch, V. Seyda, Laser additive manufacturing of modified implant surfaces with osseointegrative characteristics, Phys. Procedia 12 (2011) 375–384.
[9] C. Emmelmann, P. Sander, J. Kranz, E. Wycisk, Laser additive manufacturing and bionics: redefining lightweight design, Phys. Procedia 12 (2011) 364–368.
[10] Y.-L. Hao, S.-J. Li, R. Yang, Biomedical titanium alloys and their additive manufacturing, Rare Metals 35 (9) (2016) 661–671.
[11] J. Giannatsis, V. Dedoussis, Additive fabrication technologies applied to medicine and health care: a review, Int. J. Adv. Manuf. Technol. 40 (1) (2009) 116–127.
[12] L. Ciocca, M. Fantini, F. De Crescenzio, G. Corinaldesi, R. Scotti, Direct metal laser sintering (DMLS) of a customized titanium mesh for prosthetically guided bone regeneration of atrophic maxillary arches, Med. Biol. Eng. Comput. 49 (11) (2011) 1347–1352.
[13] I. Gurrappa, Characterization of titanium alloy Ti-6Al-4V for chemical, marine and industrial applications, Mater. Charact. 51 (2) (2003) 131–139.
[14] A.S. Oryshchenko, I.V. Gorynin, V.P. Leonov, A.S. Kudryavtsev, V.I. Mikhailov, E.V. Chudakov, Marine titanium alloys: present and future, Inorg. Mater. Appl. Res. 6 (6) (2015) 571–579.
[15] I.V. Gorynin, Titanium alloys for marine application, Mater. Sci. Eng. A 263 (2) (1999) 112–116.

[16] L. Parry, I.A. Ashcroft, R.D. Wildman, Understanding the effect of laser scan strategy on residual stress in selective laser melting through thermo-mechanical simulation, Addit. Manuf. 12 (2016) 1–15.
[17] R.K. Gupta, V.A. Kumar, C. Mathew, G.S. Rao, Strain hardening of titanium alloy Ti6Al4V sheets with prior heat treatment and cold working, Mater. Sci. Eng. A 662 (2016) 537–550.
[18] C. de Formanoir, A. Brulard, S. Vivès, G. Martin, F. Prima, S. Michotte, E. Rivière, A. Dolimont, S. Godet, A strategy to improve the work-hardening behavior of Ti–6Al–4V parts produced by additive manufacturing, Mater. Res. Lett. 5 (3) (2017) 201–208.
[19] A.V.S.R. Prasad, K. Ramji, G.L. Datta, An experimental study of wire EDM on Ti-6Al-4V alloy, Proc. Mater. Sci. 5 (2014) 2567–2576.
[20] R. Huang, M. Riddle, D. Graziano, J. Warren, S. Das, S. Nimbalkar, J. Cresko, E. Masanet, Energy and emissions saving potential of additive manufacturing: the case of lightweight aircraft components, J. Clean. Prod. 135 (2016) 1559–1570.
[21] G. Lütjering, J.C. Williams, Titanium, second ed. Springer, New York, 2007.
[22] D. Herzog, V. Seyda, E. Wycisk, C. Emmelmann, Additive manufacturing of metals, Acta Mater. 117 (2016) 371–392.
[23] W.E. Frazier, Metal additive manufacturing: a review, J. Mater. Eng. Perform. 23 (6) (2014) 1917–1928.
[24] N. Guo, M.C. Leu, Additive manufacturing: technology, applications and research needs, Front. Mech. Eng. 8 (3) (2013) 215–243.
[25] I. Gibson, D. Rosen, B. Stucker, Additive Manufacturing Technologies: 3D Printing, Rapid Prototyping, and Direct Digital Manufacturing, second ed. Springer, Berlin, 2015.
[26] G.B. Kannan, D.K. Rajendran, A review on status of research in metal additive manufacturing, Advances in 3D Printing & Additive Manufacturing Technologies, Springer, Singapore 2017, pp. 95–100.
[27] A.A. Shapiro, J.P. Borgonia, Q.N. Chen, R.P. Dillon, B. McEnerney, R. Polit-Casillas, L. Soloway, Additive manufacturing for aerospace flight applications, J. Spacecr. Rocket. 53 (5) (2016) 952–959.
[28] J. Allen, An investigation into the comparative costs of additive manufacture vs. machine from solid for aero engine parts, Cost Effective Manufacture Via Net Shape Processing, 2006 , RTO-MP-AVT-139.
[29] M. Seifi, A. Salem, J. Beuth, O. Harrysson, J.J. Lewandowski, Overview of materials qualification needs for metal additive manufacturing, JOM 68 (3) (2016) 747–764.
[30] R. O'Leary, R. Setchi, P. Prickett, G. Hankins, N. Jones, An investigation into the recycling of Ti-6Al-4V powder used within SLM to improve sustainability, SDM'2015: 2nd International Conference on Sustainable Design and Manufacturing, Seville, Spain, 2015.
[31] H. Galarraga, R.J. Warren, D.A. Lados, R.R. Dehoff, M.M. Kirka, P. Nandwana, Effects of heat treatments on microstructure and properties of Ti-6Al-4V ELI alloy fabricated by electron beam melting (EBM), Mater. Sci. Eng. A 685 (2017) 417–428.
[32] R. Yan, D. Luo, H. Huang, R. Li, N. Yu, C. Liu, M. Hu, Q. Rong, Electron beam melting in the fabrication of three-dimensional mesh titanium mandibular prosthesis scaffold, Sci. Rep. 8 (1) (2018) 750.
[33] https://slm-solutions.com/.
[34] http://www.ritspace.se/.
[35] http://tusharmahale.wixsite.com/home/obtainium.
[36] https://www.rtejournal.de/ausgabe2/233/view?set_language=en.
[37] R. Wauthle, B. Vrancken, B. Beynaerts, K. Jorissen, J. Schrooten, J.-P. Kruth, J. Van Humbeeck, Effects of build orientation and heat treatment on the microstructure and mechanical properties of selective laser melted Ti6Al4V lattice structures, Addit. Manuf. 5 (2015) 77–84.
[38] Y.C. Shin, N. Bailey, C. Katinas, W. Tan, Predictive modeling capabilities from incident powder and laser to mechanical properties for laser directed energy deposition, Comput. Mech. 61 (5) (2018) 617–636.
[39] C. Katinas, S. Liu, Y.C. Shin, Self-sufficient modeling of single track deposition of Ti–6Al–4V with the prediction of capture efficiency, J. Manuf. Sci. Eng. 141 (1) (2018) (011001-011001-10).
[40] S. Liu, Y.C. Shin, Simulation and experimental studies on microstructure evolution of resolidified dendritic TiCx in laser direct deposited Ti-TiC composite, Mater. Des. 159 (2018) 212–223.
[41] S. Tammas-Williams, H. Zhao, F. Léonard, F. Derguti, I. Todd, P.B. Prangnell, XCT analysis of the influence of melt strategies on defect population in Ti–6Al–4V components manufactured by selective electron beam melting, Mater. Charact. 102 (2015) 47–61.
[42] M. Strantza, R. Vafadari, D. de Baere, B. Vrancken, W. van Paepegem, I. Vandendael, H. Terryn, P. Guillaume, D. van Hemelrijck, Fatigue of Ti6Al4V structural health monitoring systems produced by selective laser melting, Materials (Basel) 9 (2) (2016).
[43] N. Biswas, J.L. Ding, V.K. Balla, D.P. Field, A. Bandyopadhyay, Deformation and fracture behavior of laser processed dense and porous Ti6Al4V alloy under static and dynamic loading, Mater. Sci. Eng. A 549 (2012) 213–221.
[44] S. Beretta, S. Romano, A comparison of fatigue strength sensitivity to defects for materials manufactured by AM or traditional processes, Int. J. Fatigue 94 (2017) 178–191.
[45] N. Hrabe, T. Gnäupel-Herold, T. Quinn, Fatigue properties of a titanium alloy (Ti–6Al–4V) fabricated via electron beam melting (EBM): effects of internal defects and residual stress, Int. J. Fatigue 94 (2017) 202–210.
[46] C. Qiu, N.J.E. Adkins, M.M. Attallah, Microstructure and tensile properties of selectively laser-melted and of HIPed laser-melted Ti–6Al–4V, Mater. Sci. Eng. A 578 (2013) 230–239.
[47] S. Leuders, M. Thöne, A. Riemer, T. Niendorf, T. Tröster, H.A. Richard, H.J. Maier, On the mechanical behaviour of titanium alloy TiAl6V4 manufactured by selective laser melting: fatigue resistance and crack growth performance, Int. J. Fatigue 48 (2013) 300–307.
[48] G. Kasperovich, J. Hausmann, Improvement of fatigue resistance and ductility of TiAl6V4 processed by selective laser melting, J. Mater. Process. Technol. 220 (2015) 202–214.
[49] J. Alcisto, A. Enriquez, H. Garcia, S. Hinkson, T. Steelman, E. Silverman, P. Valdovino, H. Gigerenzer, J. Foyos, J. Ogren, J. Dorey, K. Karg, T. McDonald, O.S. Es-Said, Tensile properties and microstructures of laser-formed Ti–6Al–4V, J. Mater. Eng. Perform. 20 (2) (2011) 203–212.
[50] B.J. Hayes, B.W. Martin, B. Welk, S.J. Kuhr, T.K. Ales, D.A. Brice, I. Ghamarian, A.H. Baker, C.V. Haden, D.G. Harlow, H.L. Fraser, P.C. Collins, Predicting tensile properties of Ti–6Al–4V produced via directed energy deposition, Acta Mater. 133 (2017) 120–133.
[51] B. Vrancken, L. Thijs, J.-P. Kruth, J. Van Humbeeck, Heat treatment of Ti6Al4V produced by selective laser melting: microstructure and mechanical properties, J. Alloys Compd. 541 (2012) 177–185.
[52] ASTM, ASTM F2792–10 Standard Terminology for Additive Manufacturing Technologies, 2010.
[53] M. Baumers, C. Tuck, R. Wildman, I. Ashcroft, R. Hague, Shape complexity and process energy consumption in electron beam melting: a case of something for nothing in additive manufacturing? J. Ind. Ecol. 21 (S1) (2017) S157–S167.
[54] M.J. Bermingham, L. Nicastro, D. Kent, Y. Chen, M.S. Dargusch, Optimising the mechanical properties of Ti-6Al-4V components produced by wire + arc additive manufacturing with post-process heat treatments, J. Alloys Compd. 753 (2018) 247–255.
[55] J. Zhang, X. Wang, S. Paddea, X. Zhang, Fatigue crack propagation behaviour in wire + arc additive manufactured Ti-6Al-4V: effects of microstructure and residual stress, Mater. Des. 90 (2016) 551–561.
[56] J.R. Hönnige, P.A. Colegrove, B. Ahmad, M.E. Fitzpatrick, S. Ganguly, T.L. Lee, S.W. Williams, Residual stress and texture control in Ti-6Al-4V wire + arc additively manufactured intersections by stress relief and rolling, Mater. Des. 150 (2018) 193–205.
[57] J.M. Wilson, C. Piya, Y.C. Shin, F. Zhao, K. Ramani, Remanufacturing of turbine blades by directed energy deposition with its energy and environmental impact analysis, J. Clean. Prod. 80 (2014) 170–178.
[58] B. Wysocki, P. Maj, R. Sitek, J. Buhagiar, K. Kurzydłowski, W. Święszkowski, Laser and electron beam additive manufacturing methods of fabricating titanium bone implants, Appl. Sci. 7 (7) (2017) 657 (1–20).
[59] S.M. Thompson, L. Bian, N. Shamsaei, A. Yadollahi, An overview of direct laser deposition for additive manufacturing; part I: transport phenomena, modeling and diagnostics, Addit.Manuf. 8 (2015) 36–62.
[60] J.M. Wilson, Y.C. Shin, Microstructure and wear properties of laser-deposited functionally graded Inconel 690 reinforced with TiC, Surf. Coat. Technol. 207 (2012) 517–522.
[61] S. Liu, Y.C. Shin, The influences of melting degree of TiC reinforcements on microstructure and mechanical properties of laser direct deposited Ti6Al4V-TiC composites, Mater. Des. 136 (2017) 185–195.
[62] A. Gasser, G. Backes, I. Kelbassa, A. Weisheit, K. Wissenbach, Laser additive manufacturing, Laser Tech. J. 7 (2) (2010) 58–63.
[63] R.P. Mudge, N.R. Wald, Laser engineered net shaping advances additive manufacturing and repair, Weld. J. 86 (1) (2007) 44–48.
[64] T. Petrat, B. Graf, A. Gumenyuk, M. Rethmeier, Laser metal deposition as repair technology for a gas turbine burner made of Inconel 718, Phys. Procedia 83 (2016) 761–768.
[65] http://www.dragonfly.am/?q=en/additive-technologies-mechanical-parts-repairing.
[66] L.J. Kumar, C.G.K. Nair, Laser metal deposition repair applications for Inconel 718 alloy, Mater. Today Proc. 4 (10) (2017) 11068–11077.
[67] M. Brandt, The role of lasers in additive manufacturing, in: M. Brandt (Ed.), Laser Additive Manufacturing, Woodhead Publishing 2017, pp. 1–18.
[68] L.E. Andersson, M. Larsson, Device and arrangement for producing a three-dimensional object. Patent WO 2001081031 A1, 2001.
[69] P. Li, D.H. Warner, A. Fatemi, N. Phan, Critical assessment of the fatigue performance of additively manufactured Ti–6Al–4V and perspective for future research, Int. J. Fatigue 85 (2016) 130–143.
[70] H. Weiwei, J. Wenpeng, L. Haiyan, T. Huiping, K. Xinting, H. Yu, Research on preheating of titanium alloy powder in electron beam melting technology, Rare Metal Mater. Eng. 40 (12) (2011) 2072–2075.
[71] V. Chastand, P. Quaegebeur, W. Maia, E. Charkaluk, Comparative study of fatigue properties of Ti-6Al-4V specimens built by electron beam melting (EBM) and selective laser melting (SLM), Mater. Charact. 143 (2018) 76–81.
[72] Y. Zhai, H. Galarraga, D.A. Lados, Microstructure, static properties, and fatigue crack growth mechanisms in Ti-6Al-4V fabricated by additive manufacturing: LENS and EBM, Eng. Fail. Anal. 69 (2016) 3–14.
[73] B.E. Carroll, T.A. Palmer, A.M. Beese, Anisotropic tensile behavior of Ti–6Al–4V components fabricated with directed energy deposition additive manufacturing, Acta Mater. 87 (2015) 309–320.
[74] L. Qian, J. Mei, J. Liang, X. Wu, Influence of position and laser power on thermal history and microstructure of direct laser fabricated Ti–6Al–4V samples, Mater. Sci. Technol. 21 (5) (2005) 597–605.
[75] J. Yu, M. Rombouts, G. Maes, F. Motmans, Material properties of Ti6Al4V parts produced by laser metal deposition, Phys. Procedia 39 (2012) 416–424.
[76] I. Yadroitsev, P. Krakhmalev, I. Yadroitsava, Selective laser melting of Ti6Al4V alloy for biomedical applications: temperature monitoring and microstructural evolution, J. Alloys Compd. 583 (2014) 404–409.
[77] P.K. Gokuldoss, S. Kolla, J. Eckert, Additive manufacturing processes: selective laser melting, electron beam melting and binder jetting-selection guidelines, Materials (Basel) 10 (6) (2017).

[78] C. Qiu, M.A. Kindi, A.S. Aladawi, I.A. Hatmi, A comprehensive study on microstructure and tensile behaviour of a selectively laser melted stainless steel, Sci. Rep. 8 (1) (2018) 7785.
[79] A. Safdar, L.Y. Wei, A. Snis, Z. Lai, Evaluation of microstructural development in electron beam melted Ti-6Al-4V, Mater. Charact. 65 (2012) 8–15.
[80] B. Cheng, S. Price, J. Lydon, K. Cooper, K. Chou, On process temperature in powder-bed electron beam additive manufacturing: model development and validation, J. Manuf. Sci. Eng. 136 (6) (2014), 061018. .
[81] S. Price, J. Lydon, K. Cooper, K. Chou, Experimental temperature analysis of powder-based electron beam additive manufacturing, 24th, Annual International Solid Freeform Fabrication Symposium; an Additive Manufacturing Conference, Proceedings, University of Texas, Austin, TX 2013, pp. 162–173.
[82] S.S. Al-Bermani, M.L. Blackmore, W. Zhang, I. Todd, The origin of microstructural diversity, texture, and mechanical properties in electron beam melted Ti-6Al-4V, Metall. Mater. Trans. A 41 (13) (2010) 3422–3434.
[83] A.A. Antonysamy, J. Meyer, P.B. Prangnell, Effect of build geometry on the β-grain structure and texture in additive manufacture of Ti6Al4V by selective electron beam melting, Mater. Charact. 84 (2013) 153–168.
[84] D.A. Hollander, M. von Walter, T. Wirtz, R. Sellei, B. Schmidt-Rohlfing, O. Paar, H.-J. Erli, Structural, mechanical and in vitro characterization of individually structured Ti–6Al–4V produced by direct laser forming, Biomaterials 27 (7) (2006) 955–963.
[85] E. Sallica-Leva, A.L. Jardini, J.B. Fogagnolo, Microstructure and mechanical behavior of porous Ti-6Al-4V parts obtained by selective laser melting, J. Mech. Behav. Biomed. Mater. 26 (2013) 98–108.
[86] V.K. Balla, S. Martinez, B.T. Rogoza, C. Livingston, D. Venkateswaran, S. Bose, A. Bandyopadhyay, Quasi-static torsional deformation behavior of porous Ti6Al4V alloy, Mater. Sci. Eng. C 31 (5) (2011) 945–949.
[87] T. Vilaro, C. Colin, J.D. Bartout, As-fabricated and heat-treated microstructures of the Ti-6Al-4V alloy processed by selective laser melting, Metall. Mater. Trans. A 42 (10) (2011) 3190–3199.
[88] P.-H. Li, W.-G. Guo, W.-D. Huang, Y. Su, X. Lin, K.-B. Yuan, Thermomechanical response of 3D laser-deposited Ti–6Al–4V alloy over a wide range of strain rates and temperatures, Mater. Sci. Eng. A 647 (2015) 34–42.
[89] U. Ackelid, M. Svensson, Additive manufacturing of dense metal parts by electron beam melting, Materials Science and Technology Conference, Association for Iron & Steel Technology, Pittsburgh, PA 2009, pp. 2711–2719.
[90] K. Puebla, L.E. Murr, S.M. Gaytan, E. Martinez, F. Medina, R.B. Wicker, Effect of melt scan rate on microstructure and macrostructure for electron beam melting of Ti-6Al-4V, Mater. Sci. Appl. 3 (5) (2012) 259–264.
[91] M. Seifi, M. Dahar, R. Aman, O. Harrysson, J. Beuth, J.J. Lewandowski, Evaluation of orientation dependence of fracture toughness and fatigue crack propagation behavior of as-deposited ARCAM EBM Ti-6Al-4V, JOM 67 (3) (2015) 597–607.
[92] L.E. Murr, S.M. Gaytan, A. Ceylan, E. Martinez, J.L. Martinez, D.H. Hernandez, B.I. Machado, D.A. Ramirez, F. Medina, S. Collins, R.B. Wicker, Characterization of titanium aluminide alloy components fabricated by additive manufacturing using electron beam melting, Acta Mater. 58 (5) (2010) 1887–1894.
[93] H. Galarraga, D.A. Lados, R.R. Dehoff, M.M. Kirka, P. Nandwana, Effects of the microstructure and porosity on properties of Ti-6Al-4V ELI alloy fabricated by electron beam melting (EBM), Addit. Manuf. 10 (2016) 47–57.
[94] P.A. Kobryn, E.H. Moore, S.L. Semiatin, The effect of laser power and traverse speed on microstructure, porosity, and build height in laser-deposited Ti-6Al-4V, Scr. Mater. 43 (4) (2000) 299–305.
[95] Y. Yang, H.C. Man, Microstructure evolution of laser clad layers of W–C–Co alloy powders. This paper is sponsored by The Natural Science Foundation of Guangdong Province, China, Surf. Coat. Technol. 132 (2) (2000) 130–136.
[96] A. Bauereiß, T. Scharowsky, C. Körner, Defect generation and propagation mechanism during additive manufacturing by selective beam melting, J. Mater. Process. Technol. 214 (11) (2014) 2522–2528.
[97] G.K.L. Ng, A.E.W. Jarfors, G. Bi, H.Y. Zheng, Porosity formation and gas bubble retention in laser metal deposition, Appl. Phys. A 97 (3) (2009) 641–649.
[98] J. Choi, Y. Chang, Characteristics of laser aided direct metal/material deposition process for tool steel, Int. J. Mach. Tools Manuf. 45 (4–5) (2005) 597–607.
[99] C. de Formanoir, S. Michotte, O. Rigo, L. Germain, S. Godet, Electron beam melted Ti–6Al–4V: microstructure, texture and mechanical behavior of the as-built and heat-treated material, Mater. Sci. Eng. A 652 (2016) 105–119.
[100] S.M. Gaytan, L.E. Murr, F. Medina, E. Martinez, M.I. Lopez, R.B. Wicker, Advanced metal powder based manufacturing of complex components by electron beam melting, Mater. Technol. 24 (3) (2009) 180–190.
[101] E. Wycisk, A. Solbach, S. Siddique, D. Herzog, F. Walther, C. Emmelmann, Effects of defects in laser additive manufactured Ti-6Al-4V on fatigue properties, Phys. Procedia 56 (2014) 371–378.
[102] Y. Li, H. Yang, X. Lin, W. Huang, J. Li, Y. Zhou, The influences of processing parameters on forming characterizations during laser rapid forming, Mater. Sci. Eng. A 360 (1) (2003) 18–25.
[103] H.K. Rafi, N.V. Karthik, H. Gong, T.L. Starr, B.E. Stucker, Microstructures and mechanical properties of Ti6Al4V parts fabricated by selective laser melting and electron beam melting, J. Mater. Eng. Perform. 22 (12) (2013) 3872–3883.
[104] M. Hinderdael, M. Strantza, D. De Baere, W. Devesse, I. De Graeve, H. Terryn, P. Guillaume, Fatigue performance of Ti-6Al-4V additively manufactured specimens with integrated capillaries of an embedded structural health monitoring system, Materials (Basel) 10 (9) (2017) 1–19.
[105] R.M. Mahamood, E.T. Akinlabi, Effect of laser power on surface finish during laser metal deposition process, Proceedings of the World Congress on Engineering and Computer Science (WCECS), San Francisco, USA, 2014.
[106] H. Gong, K. Rafi, H. Gu, G.D. Janaki Ram, T. Starr, B. Stucker, Influence of defects on mechanical properties of Ti–6Al–4V components produced by selective laser melting and electron beam melting, Mater. Des. 86 (2015) 545–554.
[107] X. Zhao, S. Li, M. Zhang, Y. Liu, T.B. Sercombe, S. Wang, Y. Hao, R. Yang, L.E. Murr, Comparison of the microstructures and mechanical properties of Ti–6Al–4V fabricated by selective laser melting and electron beam melting, Mater. Des. 95 (2016) 21–31.
[108] P. Edwards, M. Ramulu, Fatigue performance evaluation of selective laser melted Ti–6Al–4V, Mater. Sci. Eng. A 598 (2014) 327–337.
[109] K.S. Chan, M. Koike, R.L. Mason, T. Okabe, Fatigue life of titanium alloys fabricated by additive layer manufacturing techniques for dental implants, Metall. Mater. Trans. A 44 (2) (2013) 1010–1022.
[110] B. Vayssette, N. Saintier, C. Brugger, M. Elmay, E. Pessard, Surface roughness of Ti-6Al-4V parts obtained by SLM and EBM: effect on the high cycle fatigue life, Proc. Eng. 213 (2018) 89–97.
[111] M. Resch, A.F.H. Kaplan, D. Schuoecker, Laser-assisted generating of three-dimensional parts by the blown powder process, 4184 (2001) 555–558.
[112] A.F.H. Kaplan, G. Groboth, Process analysis of laser beam cladding, J. Manuf. Sci. Eng. 123 (4) (2000) 609–614.
[113] J. Mazumder, D. Dutta, N. Kikuchi, A. Ghosh, Closed loop direct metal deposition: art to part, Opt. Lasers Eng. 34 (4) (2000) 397–414.
[114] J.H. Shaikh, N.K. Jain, V.C. Venkatesh, Precision finishing of bevel gears by electrochemical honing, Mater. Manuf. Process. 28 (10) (2013) 1117–1123.
[115] G. Vastola, G. Zhang, Q.X. Pei, Y.W. Zhang, Controlling of residual stress in additive manufacturing of Ti6Al4V by finite element modeling, Addit. Manuf. 12 (2016) 231–239.
[116] N.S. Bailey, W. Tan, Y.C. Shin, Predictive modeling and experimental results for residual stresses in laser hardening of AISI 4140 steel by a high power diode laser, Surf. Coat. Technol. 203 (14) (2009) 2003–2012.
[117] N.S. Bailey, C. Katinas, Y.C. Shin, Directed energy deposition of AISI H13 tool steel powder with numerical modeling of solid phase transformation, hardness, and residual stresses, J. Mater. Process. Technol. 247 (2017) 223–233.
[118] S. Bontha, N. Klingbeil, Thermal process maps for controlling microstructure in laser-based solid freeform fabrication, Solid Freeform Fabrication Proceedings 2003, pp. 219–226.
[119] P. Mercelis, J.P. Kruth, Residual stresses in selective laser sintering and selective laser melting, Rapid Prototyp. J. 12 (5) (2006) 254–265.
[120] Y. Liu, Y. Yang, D. Wang, A study on the residual stress during selective laser melting (SLM) of metallic powder, Int. J. Adv. Manuf. Technol. 87 (1) (2016) 647–656.
[121] L.D. Bobbio, S. Qin, A. Dunbar, P. Michaleris, A.M. Beese, Characterization of the strength of support structures used in powder bed fusion additive manufacturing of Ti-6Al-4V, Addit. Manuf. 14 (2017) 60–68.
[122] J.-P. Järvinen, V. Matilainen, X. Li, H. Piili, A. Salminen, I. Mäkelä, O. Nyrhilä, Characterization of effect of support structures in laser additive manufacturing of stainless steel, Phys. Procedia 56 (2014) 72–81.
[123] D. Banerjee, J.C. Williams, Perspectives on titanium science and technology, Acta Mater. 61 (3) (2013) 844–879.
[124] J. Yang, H. Yu, J. Yin, M. Gao, Z. Wang, X. Zeng, Formation and control of martensite in Ti-6Al-4V alloy produced by selective laser melting, Mater. Des. 108 (2016) 308–318.
[125] D. Agius, K. Kourousis, C. Wallbrink, A review of the as-built SLM Ti-6Al-4V mechanical properties towards achieving fatigue resistant designs, Metals 8 (1) (2018) 75 (1–25).
[126] W. Xu, S. Sun, J. Elambasseril, Q. Liu, M. Brandt, M. Qian, Ti-6Al-4V additively manufactured by selective laser melting with superior mechanical properties, JOM 67 (3) (2015) 668–673.
[127] A. Ducato, L. Fratini, M. La Cascia, G. Mazzola, An Automated Visual Inspection System for the Classification of the Phases of Ti-6Al-4V Titanium Alloy, Springer Berlin Heidelberg, Berlin, Heidelberg, 2013 362–369.
[128] T. Ahmed, H.J. Rack, Phase transformations during cooling in α + β titanium alloys, Mater. Sci. Eng. A 243 (1) (1998) 206–211.
[129] Materials Properties Handbook: Titanium Alloys. , ASM International, Materials Park, OH, 1994.
[130] F.X. Gil Mur, D. Rodríguez, J.A. Planell, Influence of tempering temperature and time on the α′-Ti-6Al-4V martensite, J. Alloys Compd. 234 (2) (1996) 287–289.
[131] U. Reisgen, S. Olschok, R. Sharma, S. Gach, Influence on martensite-start-temperature and volume expansion of low-transformation-temperature materials used for residual stress relief in beam welding, Mater. Werkst. 48 (12) (2017) 1276–1282.
[132] M. Koike, P. Greer, K. Owen, G. Lilly, L.E. Murr, S.M. Gaytan, E. Martinez, T. Okabe, Evaluation of titanium alloys fabricated using rapid prototyping technologies-electron beam melting and laser beam melting, Materials (Basel) 4 (10) (2011) 1776–1792.
[133] N. Hrabe, T. Quinn, Effects of processing on microstructure and mechanical properties of a titanium alloy (Ti–6Al–4V) fabricated using electron beam melting (EBM), part 2: energy input, orientation, and location, Mater. Sci. Eng. A 573 (2013) 271–277.
[134] M. Simonelli, Y.Y. Tse, C. Tuck, The formation of α + β microstructure in as-fabricated selective laser melting of Ti–6Al–4V, J. Mater. Res. 29 (17) (2014) 2028–2035.
[135] R.K. Nalla, R.O. Ritchie, B.L. Boyce, J.P. Campbell, J.O. Peters, Influence of microstructure on high-cycle fatigue of Ti-6Al-4V: bimodal vs. lamellar structures, Metall. Mater. Trans. A 33 (3) (2002) 899–918.
[136] J. Liu, Y. Jin, X. Fang, C. Chen, Q. Feng, X. Liu, Y. Chen, T. Suo, F. Zhao, T. Huang, H. Wang, X. Wang, Y. Fang, Y. Wei, L. Meng, J. Lu, W. Yang, Dislocation strengthening without ductility trade-off in metastable austenitic steels, Sci. Rep. 6 (2016) 35345.

[137] K.-M. Hong, Y.C. Shin, Analysis of microstructure and mechanical properties change in laser welding of Ti6Al4V with a multiphysics prediction model, J. Mater. Process. Technol. 237 (2016) 420–429.
[138] J.D. Hahn, Y.C. Shin, M.J.M. Krane, Laser transformation hardening of Ti–6Al–4V in solid state with accompanying kinetic model, Surf. Eng. 23 (2) (2007) 78–82.
[139] T. Wang, Y.Y. Zhu, S.Q. Zhang, H.B. Tang, H.M. Wang, Grain morphology evolution behavior of titanium alloy components during laser melting deposition additive manufacturing, J. Alloys Compd. 632 (2015) 505–513.
[140] L. Thijs, F. Verhaeghe, T. Craeghs, J.V. Humbeeck, J.-P. Kruth, A study of the microstructural evolution during selective laser melting of Ti–6Al–4V, Acta Mater. 58 (9) (2010) 3303–3312.
[141] M. Simonelli, Y.Y. Tse, C. Tuck, Effect of the build orientation on the mechanical properties and fracture modes of SLM Ti–6Al–4V, Mater. Sci. Eng. A 616 (2014) 1–11.
[142] X. Wu, J. Liang, J. Mei, C. Mitchell, P.S. Goodwin, W. Voice, Microstructures of laser-deposited Ti–6Al–4V, Mater. Des. 25 (2) (2004) 137–144.
[143] R.J. Moat, A.J. Pinkerton, L. Li, P.J. Withers, M. Preuss, Crystallographic texture and microstructure of pulsed diode laser-deposited Waspaloy, Acta Mater. 57 (4) (2009) 1220–1229.
[144] F. Wang, J. Mei, H. Jiang, X. Wu, Laser fabrication of Ti6Al4V/TiC composites using simultaneous powder and wire feed, Mater. Sci. Eng. A 445–446 (2007) 461–466.
[145] Ø. Gong, Metallurgical Modelling of Welding (Materials Modelling Series), second ed. The Institute of Materials, London, 1997.
[146] G.P. Dinda, L. Song, J. Mazumder, Fabrication of Ti-6Al-4V scaffolds by direct metal deposition, Metall. Mater. Trans. A 39 (12) (2008) 2914–2922.
[147] E. Amsterdam, G.A. Kool, High Cycle Fatigue of Laser Beam Deposited Ti-6Al-4V and Inconel 718, Springer Netherlands, Dordrecht, 2009 1261–1274.
[148] L. Facchini, E. Magalini, P. Robotti, A. Molinari, S. Höges, K. Wissenbach, Ductility of a Ti-6Al-4V alloy produced by selective laser melting of prealloyed powders, Rapid Prototyp. J. 16 (6) (2010) 450–459.
[149] P. Edwards, A. O'Conner, M. Ramulu, Electron beam additive manufacturing of titanium components: properties and performance, J. Manuf. Sci. Eng. 135 (6) (2013), 061016. .
[150] H. Carreon, A. Ruiz, B. Santoveña, Study of aging effects in a Ti-6AL-4V alloy with Widmanstätten and equiaxed microstructures by non-destructive means, AIP Conf. Proc. 1581 (1) (2014) 739–745.
[151] S. Guo, Q. Meng, G. Liao, L. Hu, X. Zhao, Microstructural evolution and mechanical behavior of metastable β-type Ti–25Nb–2Mo–4Sn alloy with high strength and low modulusMicrostructural evolution and mechanical behavior of metastable β-type Ti–25Nb–2Mo–4Sn alloy with high strength and low modulusretain, Prog. Nat. Sci. Mater. Int. 23 (2) (2013) 174–182.
[152] J. Sieniawski, W. Ziaja, K. Kubiak, M. Motyk, Microstructure and mechanical properties of high strength two-phase titanium alloys, in: J. Sieniawski, W. Ziaja (Eds.), Titanium Alloys-Advances in Properties Control, IntechOpen 2013, pp. 69–80.
[153] X. Li, J. Xie, Y. Zhou, Effects of oxygen contamination in the argon shielding gas in laser welding of commercially pure titanium thin sheet, J. Mater. Sci. 40 (13) (2005) 3437–3443.
[154] H. Conrad, Effect of interstitial solutes on the strength and ductility of titanium, Prog. Mater. Sci. 26 (2) (1981) 123–403.
[155] A.A. Shanyavskiy, Very-high-cycle-fatigue of in-service air-engine blades, compressor and turbine, Sci. China Phys. Mech. Astron. 57 (1) (2014) 19–29.
[156] R. Grylls, LENS Process White Paper: Fatigue Testing of LENS Ti-6-4, OPTOMEC, 2005 1–5.
[157] A.W. Prabhu, T. Vincent, A. Chaudhary, W. Zhang, S.S. Babu, Effect of microstructure and defects on fatigue behaviour of directed energy deposited Ti–6Al–4V, Sci. Technol. Weld. Join. 20 (8) (2015) 659–669.
[158] M. Seifi, A. Salem, D. Satko, J. Shaffer, J.J. Lewandowski, Defect distribution and microstructure heterogeneity effects on fracture resistance and fatigue behavior of EBM Ti–6Al–4V, Int. J. Fatigue 94 (2017) 263–287.
[159] T.M. Mower, M.J. Long, Mechanical behavior of additive manufactured, powder-bed laser-fused materials, Mater. Sci. Eng. A 651 (2016) 198–213.
[160] B. Oberwinkler, M. Riedler, W. Eichlseder, Importance of local microstructure for damage tolerant light weight design of Ti–6Al–4V forgings, Int. J. Fatigue 32 (5) (2010) 808–814.
[161] G. Léopold, Y. Nadot, T. Billaudeau, J. Mendez, Influence of artificial and casting defects on fatigue strength of moulded components in Ti-6Al-4V alloy, Fatigue Fract. Eng. Mater. Struct. 38 (9) (2015) 1026–1041.
[162] S. Tammas-Williams, P.J. Withers, I. Todd, P.B. Prangnell, The influence of porosity on fatigue crack initiation in additively manufactured titanium components, Sci. Rep. 7 (1) (2017) 7308.
[163] J. Günther, D. Krewerth, T. Lippmann, S. Leuders, T. Tröster, A. Weidner, H. Biermann, T. Niendorf, Fatigue life of additively manufactured Ti–6Al–4V in the very high cycle fatigue regime, Int. J. Fatigue 94 (2017) 236–245.
[164] L.E. Murr, S.A. Quinones, S.M. Gaytan, M.I. Lopez, A. Rodela, E.Y. Martinez, D.H. Hernandez, E. Martinez, F. Medina, R.B. Wicker, Microstructure and mechanical behavior of Ti-6Al-4V produced by rapid-layer manufacturing, for biomedical applications, J. Mech. Behav. Biomed. Mater. 2 (1) (2009) 20–32.
[165] G. Lütjering, A. Gysler, Fatigue: A critical review, in: G. Lütjering, U. Zwicker, W. Bunk (Eds.),Titanium'84: Science and Technology, Proc. 5th World Conference on Titanium, Munich, Germany, September 1984, Deutsche Gesellschaft fur Metallkunde E.V., 1985, pp. 2065–2083.
[166] A.K. Polasik, The Role of Microstructure on High Cycle Fatigue Lifetime Variability in Ti-6Al-4V, (Doctoral thesis) The Ohio State University, OH, USA, 2014.
[167] I. Bantounas, D. Dye, T.C. Lindley, The role of microtexture on the faceted fracture morphology in Ti–6Al–4V subjected to high-cycle fatigue, Acta Mater. 58 (11) (2010) 3908–3918.
[168] S. Heinz, F. Balle, G. Wagner, D. Eifler, Analysis of fatigue properties and failure mechanisms of Ti6Al4V in the very high cycle fatigue regime using ultrasonic technology and 3D laser scanning vibrometry, Ultrasonics 53 (8) (2013) 1433–1440.
[169] M. Suraratchai, J. Limido, C. Mabru, R. Chieragatti, Modelling the influence of machined surface roughness on the fatigue life of aluminium alloy, Int. J. Fatigue 30 (12) (2008) 2119–2126.
[170] E. Wycisk, C. Emmelmann, S. Siddique, F. Walther, High cycle fatigue (HCF) performance of Ti-6Al-4V alloy processed by selective laser melting, Adv. Mater. Res. 816–817 (2013) 134–139.
[171] D. Greitemeier, C. Dalle Donne, F. Syassen, J. Eufinger, T. Melz, Effect of surface roughness on fatigue performance of additive manufactured Ti–6Al–4V, Mater. Sci. Technol. 32 (7) (2016) 629–634.
[172] Z. Xu, W. Wen, T. Zhai, Effects of pore position in depth on stress/strain concentration and fatigue crack initiation, Metall. Mater. Trans. A 43 (8) (2012) 2763–2770.
[173] Y. Murakami, Material defects as the basis of fatigue design, Int. J. Fatigue 41 (2012) 2–10.
[174] P.J. Golden, R. John, W.J. Porter, Investigation of variability in fatigue crack nucleation and propagation in alpha + beta Ti-6Al-4V, Proc. Eng. 2 (1) (2010) 1839–1847.
[175] L. Wagner, Mechanical surface treatments on titanium, aluminum and magnesium alloys, Mater. Sci. Eng. A 263 (2) (1999) 210–216.